Journal of Computational Physics 229 (2010) 2773–2809

Contents lists available at ScienceDirect

Journal of Computational Physics

journal homepage: www.elsevier.com/locate/jcp

An anti-diffusive numerical scheme for the simulation of interfaces between compressible fluids by means of a five-equation model

S. Kokh [a,*], F. Lagoutière [b,c]

[a] DEN/DANS/DM2S/SFME/LETR, CEA Saclay, 91191 Gif-sur-Yvette Cedex, France
[b] Université Paris-Sud 11, Département de Mathématiques, Bâtiment 425, 91405 Orsay Cedex, France
[c] Équipe-Projet SIMPAF, Centre de Recherche INRIA Futurs, Parc Scientifique de la Haute Borne, 40, Avenue Halley B.P. 70478, F-59658 Villeneuve d'Ascq Cedex, France

ARTICLE INFO

Article history:
Received 3 October 2008
Received in revised form 21 October 2009
Accepted 1 December 2009
Available online 4 January 2010

Keywords:
Multi-component flows
Interface problems
Numerical diffusion
Compressible flows
Real fluids

ABSTRACT

We propose a discretization method of a five-equation model with isobaric closure for the simulation of interfaces between compressible fluids. This numerical solver is a Lagrange–Remap scheme that aims at controlling the numerical diffusion of the interface between both fluids. This method does not involve any interface reconstruction procedure. The solver is equipped with built-in stability and consistency properties and is conservative with respect to mass, momentum, total energy and partial masses. This numerical scheme works with a very broad range of equations of state, including tabulated laws. Properties that ensure a good treatment of the Riemann invariants across the interface are proven. As a consequence, the numerical method does not create spurious pressure oscillations at the interface. We show one-dimensional and two-dimensional classic numerical tests. The results are compared with the approximate solutions obtained with the classic upwind Lagrange–Remap approach, and with experimental and previously published results of a reference test case.

1. Introduction

We consider the simulation of flows with interfaces separating two compressible fluids. A first classic approach consists in modelling the flow of each fluid by the compressible Euler equations in each fluid domain and then coupling both systems across the interface thanks to jump relations. This coupling formulation can be replaced by an alternate single problem defined over the whole computational domain by introducing an additional parameter generally called a "color function". The color function can be a physically relevant parameter, e.g. a mass fraction of a volume fraction, or an abstract parameter that takes the value 0 (resp. 1) in fluid 0 (resp. 1). The system can thus be viewed as the flow of a single equivalent fluid whose state law is defined according to the value of the color function. In this case, the material interface is located by the discontinuity locus of the color function. This framework has been used extensively for the past years and has contributed to popularize interface capture methods. The ground of interface capture methods consists in solving an evolution PDE for the color function without any interface reconstruction process. This usually creates a numerical transition zone for the color function that requires to introduce a mixture model. Indeed, for compressible fluids, although we suppose both fluids to be equipped with their own Equation of State (EOS), no EOS is given *a priori* for the region where the interface becomes numerically smeared.

Among the numerous works that have addressed this issue, we choose here to focus on the five-equation system proposed in [2,3] that provides a convenient model for the EOS in the numerical transition zone. Let us mention that other five-equation systems have been studied by [20,21,24] for the case of more complex interface problems that account for physical mixing zones. These works usually propose a discretization based on an approximate Riemann solver. Unfortunately

* Corresponding author. Tel.: +33 1 6908 8568.
E-mail addresses: samuel.kokh@cea.fr (S. Kokh), frederic.lagoutiere@math.u-psud.fr (F. Lagoutière).

0021-9991/$ - see front matter © 2009 Elsevier Inc. All rights reserved.
doi:10.1016/j.jcp.2009.12.003

the numerical diffusion generated by the solvers tends to extend the smeared zone that captures the interface. As a consequence, for simulations that require a relatively large amount of time steps the interface shape may no longer be distinguishable. A possible cure for this drawback is to consider interface capture methods such as the well-known level set methods [47,30,31,9,46,45] which intrinsically do not smear the interface. Instead of capturing the profile of a discontinuous color function, level set methods propose to define the interface as the zero-level set of a function that approximates the signed distance to the interface in a neighborhood of the latter. The implementation of a level set method consists then in following the evolution of a continuous level set function thanks to a PDE instead of a discontinuous color function. However, the level set methods do not ensure the resulting algorithm to be conservative in the general case. Moreover, it requires the use of additional treatments in order to reinitialize the level set function during the computation. Both of these issues have been widely examined by numerous works. Let us mention for example [48,42,50,51,39] for conservativity issues and the work of [22,30,23,54,36,52] for reinitialization techniques.

An alternate approach to cope with the numerical smearing of the interfaces has been considered by [8]. The core of the method relies on a stability analysis initially developed for the simple case of the linear advection equation [6,19]. An extension to the capture of an interface for a specific compressible multimaterial flow model was then derived in [8] by means of a Lagrange–Remap strategy. Let us also mention the work [38] that used the linear advection scheme of [6,19] for simulating a specific system dedicated to flows with interfaces in the low-Mach regime.

Following the way paved by [19,7,8] the present paper proposes a Lagrange–Remap solver for the five-equation model of [2,3] that complies with the following constraint: the solver should be conservative with respect to partial masses, momentum, mass and total energy. Moreover one can show that for a wide range of flow configurations the solver will provide for both mass fraction and color function stability properties that are comparable to those of the classic upwind solver. The solver also provides a good treatment of the Riemann invariants across the material front in a similar way to the solver proposed in [2,3]. Let us also emphasize that our scheme does not require any additional CPU cost compared to a classic upwind Lagrange–Remap method.

The overall construction principle of our numerical scheme has been presented in [43] along with a few preliminary simulations. We intend to provide here a thorough presentation of this numerical scheme and its properties along with detailed numerical results. The paper is organized as follows: in the first section we recall the five-equation model with isobaric closure of [2,3] and its main properties, then in Section 3.1.2 we recall the general structure of a Lagrange–Remap solver. In Section 3.1.4 we show that, following our lines, the design of the whole solver boils down to properly define a numerical flux for the color function. This matter is examined in Section 3.2 where we provide stability and consistency constraints for the numerical flux associated with the color function and show that all of these constraints are compatible with each other. In Section 3.4 we present the full algorithm. We examine in Section 4 the effect of our scheme on the Riemann invariants across the material interface. Finally, we present in Section 5 a series of one-dimensional and two-dimensional numerical tests that show the good behavior of the scheme regarding the numerical diffusion of the interface.

2. The five-equation system with isobaric closure

We briefly recall in this section the system we are concerned with and its main properties. The notations we shall use here slightly differ from the original notations of [2,3].

We note ρ_k, ε_k and P_k, respectively, the density, the specific internal energy and the pressure of fluid $k = 0, 1$. We suppose each fluid $k = 0, 1$ to be equipped with an equation of state (EOS) of the form $\rho_k\varepsilon_k : (\rho_k, P_k) \mapsto \rho_k\varepsilon_k$. The position of the interface is located thanks to a color function $(x, t) \mapsto z$ that takes the value 1 (resp. 0) when the point x belongs to a pure fluid 1 (resp. 0) region at instant t.

The density ρ and specific energy ε of the two-fluid medium are given by

$$\rho = z\rho_1 + (1 - z)\rho_0, \quad \rho\varepsilon = z\rho_1\varepsilon_1 + (1 - z)\rho_0\varepsilon_0.$$

We define the mass fraction y_k of the fluid $k = 0, 1$ by setting

$$y = z\rho_1/\rho, \quad y_1 = y, \quad y_0 = 1 - y.$$

Both fluids are supposed to have the same velocity $\mathbf{u}$ and we note $e = \varepsilon + |\mathbf{u}|^2/2$ the specific total energy of the two-fluid medium. For $k = 0, 1$ let us also note $\xi_k = \rho_k(\partial\varepsilon_k/\partial P_k)_{\rho_k}$ and c_k the sound velocity of pure fluid k assumed to be real valued.

The five-equation system with isobaric closure reads

$$\begin{cases} \dfrac{\partial \rho y}{\partial t} + \operatorname{div}(\rho y \mathbf{u}) = 0, \\ \dfrac{\partial \rho}{\partial t} + \operatorname{div}(\rho \mathbf{u}) = 0, \\ \dfrac{\partial \rho \mathbf{u}}{\partial t} + \operatorname{div}(\rho \mathbf{u} \otimes \mathbf{u}) + \operatorname{grad} P = 0, \\ \dfrac{\partial \rho e}{\partial t} + \operatorname{div}[(\rho e + P)\mathbf{u}] = 0, \\ \dfrac{\partial z}{\partial t} + \mathbf{u} \cdot \mathbf{grad}\, z = 0, \end{cases} \tag{1}$$

where the pressure law $P:(\rho_0(1-z),\rho_1 z,\rho\varepsilon,z)\mapsto P$ is defined as the solution of the system

$$\begin{cases} P = P_1(\rho_1,\rho_1\varepsilon_1) = P_0(\rho_0,\rho_0\varepsilon_0), \\ \rho\varepsilon = z\rho_1\varepsilon_1 + (1-z)\rho_0\varepsilon_0 \end{cases} \tag{2}$$

for given values of ρ_0,ρ_1,z and ε. System (2) provides a consistent definition of P for a very wide class of fluids. Indeed, one can state that if the EOS of each pure fluid $k=0,1$ verifies

$$\xi_k > 0, \quad P_k \geqslant 0, \quad (\rho_k,\rho_k\varepsilon_k)\mapsto P_k \text{ is a } \mathscr{C}^1 \text{ function such that } P_k(\rho_k,\rho_k\varepsilon_k=0)=0,$$

then (2) has a unique solution (see [2,3]). Moreover, for a wide range of fluids such as Mie-Grüneisen materials, van der Waals fluids, stiffened gases or perfect gases, system (2) admits a unique solution P that can be expressed explicitly by means of the variables ρ_0,ρ_1,z and ε. Let us note that solving (2) also enables to retrieve the phasic energies $\rho_k\varepsilon_k$ thanks to the pure fluid EOSs by setting $\rho_k\varepsilon_k = \rho_k\varepsilon_k(\rho_k,P)$, where P is the solution of (2), for $k=0,1$.

Remark 1. When $z=0$ (resp. $z=1$), the closure law defined by (2) may be ambiguous as ρ_1 (resp. ρ_0) becomes an arbitrary parameter. In this case, we use a threshold value $\eta>0$ as follows: when $z<\eta$ (resp. $1-\eta<z$) we set $P=P_0(\rho,\rho\varepsilon)$ (resp. $P=P_1(\rho,\rho\varepsilon)$). When $\eta<z<1-\eta$ we retrieve P by solving (2). In practice we use $\eta=10^{-5}$, but we did not experience a significant sensitivity of the simulation results when choosing smaller values for η. Let us also note that for stiffened gases or perfect gases, the explicit definition of P degenerates naturally when z tends to 0 (resp. 1), therefore in these cases no threshold is needed.

Let us now briefly recall the eigenstructure of the five-equation system with isobaric closure. For one-dimensional problems, smooth solutions of system (1) verify the following quasi-linear system:

$$\partial_t\begin{bmatrix}\rho\mathbf{V}\\ z\end{bmatrix} + A(\rho\mathbf{V},z)\partial_x\begin{bmatrix}\rho\mathbf{V}\\ z\end{bmatrix} = 0, \quad \rho\mathbf{V} = (\rho y,\rho,\rho u,\rho e)^T. \tag{3}$$

We now recall the main well-posedness property of system (3).

Proposition 2.1. *Suppose that $\xi_1>0$ and $\xi_2>0$, then the matrix $A(\rho\mathbf{V},z)$ possesses 5 real eigenvalues $\{u-c,u,u,u,u+c\}$, where the sound velocity c of system (3) verifies*

$$\xi = z\xi_1 + (1-z)\xi_0, \quad \rho\xi c^2 = z\rho_1\xi_1 c_1^2 + (1-z)\rho_0\xi_0 c_0^2.$$

Moreover the matrix $A(\rho\mathbf{V},z)$ also possesses a set of eigenvectors that spans $\mathbb{R}^5$. Therefore system (3) is hyperbolic. The fields associated with the eigenvalues $u\pm c$ are genuinely non-linear and the fields associated with the multiple eigenvalue u are linearly degenerate.

Remark 2. System (1) can be expressed in an equivalent fully conservative form using the variables $(\rho y,\rho,\rho\mathbf{u},\rho e,\rho z)^T$. Indeed, the variable z is only allowed to experience a jump across the material interface which is associated with the linearly degenerate field. This ensures that the non-conservative product $\mathbf{u}\cdot\operatorname{grad} z$ is unambiguously defined and that the advection equation for z in system (1) can be replaced by the conservation equation: $\partial_t(\rho z) + \operatorname{div}(\rho z\mathbf{u}) = 0$.

Remark 3. The initial data for the type of problems we are concerned with do not contain $0<z<1$ values. Thus, as the variable z is passively advected by the flow through the contact discontinuity associated with u, the exact solution of system (1) will not produce any value $0<z<1$ for $t>0$. However, the discrete approximation will develop a numerical mixture zone for the discretized variable z, which is *a priori* not physically relevant in this case. This mixture zone shall converge to the zero-thickness locus of discontinuity of the variable z as the discretization space step tends to zero.

In the sequel we shall always suppose the EOS of both fluids to match hypotheses that guarantee hyperbolicity for system (3) and that provide a consistent definition of the pressure P. More specifically we shall assume that for any given values of $\rho_0>0,\rho_1>0,0<z<1$ and $\varepsilon>0$, there is a unique pressure P verifying the isobaric closure (2) and unique phasic energies values $\rho_1\varepsilon_1$ and $\rho_0\varepsilon_0$ such that $\rho\varepsilon = z\rho_1\varepsilon_1 + (1-z)\rho_0\varepsilon_0$.

3. Numerical scheme

We first present a general structure for the algorithm by briefly recalling the Lagrange–Remap process for the special case of the five-equation system with isobaric closure. While the Lagrange step is standard, we shall detail how to build a convenient Remap step that ensures two types of features. First, it provides some consistency and stability properties for the scheme. Second, it allows to minimize the diffusion of the variables which are used to locate the interface.

3.1. General quasi-conservative Lagrange-Remap form for the one-dimensional five-equation system

3.1.1. Five-equation system in Lagrangian coordinates

Let us first recall the expression of system (3) in Lagrangian coordinates. If we note $\mathrm{D}_t\cdot = \partial_t\cdot + u\partial_x\cdot$ the material derivative, then considering smooth solutions the system (3) also reads

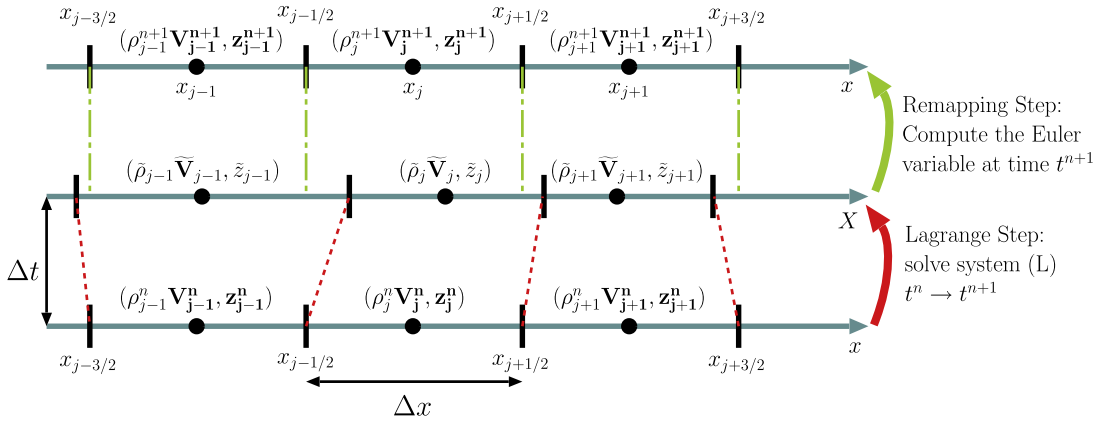

Fig. 1. Multi-step structure of the Lagrange–Remap numerical scheme.

$$
\begin{aligned}
&\rho \mathrm{D}_t y = 0,\\
&\rho \mathrm{D}_t \tau - \partial_x u = 0,\\
&\rho \mathrm{D}_t u + \partial_x P = 0,\\
&\rho \mathrm{D}_t e + \partial_x (Pu) = 0,\\
&\rho \mathrm{D}_t z = 0,
\end{aligned}
\tag{4}
$$

where $\tau = 1/\rho$. The Lagrangian coordinates system (X,t) attached to the initial instant $t=0$ is defined by

$$
X = \chi^{-1}(x,t), \quad \begin{cases} \frac{\partial}{\partial t}\chi(X,t) = u(\chi(X,t),t), \\ \chi(X,t=0) = X, \end{cases}
\tag{5}
$$

which states that $x = \chi(X,t)$ is the position at time t of the particle that was at the coordinates X at instant $t=0$. Equivalently we can say that $X = \chi^{-1}(x,t)$ is the initial position at $t=0$ of the particle that is located at the position x at the instant t. If one considers any Eulerian field $q:(x,t)\mapsto q$, then we can define a Lagrangian field $q^{\mathrm{Lag}}:(X,T)\mapsto q^{\mathrm{Lag}}(X,t)$ by setting $q^{\mathrm{Lag}}(X,t) = q(\chi(X,t),t)$ and also $q_0^{\mathrm{Lag}}(X) = q_0{}^{\mathrm{Lag}}(X,t=0) = q(\chi(X,t=0),t=0)$. Using these notation system (4) is thus equivalent to

$$
\begin{aligned}
&\rho_0^{\mathrm{Lag}} \partial_t y^{\mathrm{Lag}} = 0,\\
&\rho_0^{\mathrm{Lag}} \partial_t \tau^{\mathrm{Lag}} - \partial_X u^{\mathrm{Lag}} = 0,\\
&\rho_0^{\mathrm{Lag}} \partial_t u^{\mathrm{Lag}} + \partial_X P^{\mathrm{Lag}} = 0,\\
&\rho_0^{\mathrm{Lag}} \partial_t e^{\mathrm{Lag}} + \partial_X (P^{\mathrm{Lag}} u^{\mathrm{Lag}}) = 0,\\
&\rho_0^{\mathrm{Lag}} \partial_t z^{\mathrm{Lag}} = 0.
\end{aligned}
\tag{6}
$$

3.1.2. The Lagrange–Remap solver

We now recall the Lagrange–Remap procedure. For a detailed presentation of this algorithm the reader can refer to [11]. Let us introduce some classic notations: let $q:(x,t)\mapsto q(x,t)$ be any Eulerian field, we denote by q_j^n an approximate value of

$$
\frac{1}{\Delta x}\int_{x_{j-1/2}}^{x_{j+1/2}} q(x,t^n)\mathrm{d}x, \quad j\in\mathbb{Z}, \quad n\in\mathbb{N},
$$

where Δx is the space step and $x_j = j\Delta x, x_{j+1/2} = (j+1/2)\Delta x$. The real interval $[x_{j-1/2}, x_{j+1/2}]$ will be referred to as cell j, or cell centered in x_j. We shall note $(q_j^n)_{j\in\mathbb{Z}} = (q^n)$.

We consider a single time step from the instant t^n to the instant t^{n+1}. Let $(\rho^n\mathbf{V}^n, z^n)$ be the discretized state variable at time t^n. The Lagrange–Remap solver consists in performing the three following steps (see Fig. 1).

Step 1. Consider a Lagrangian coordinates system attached to the instant $t=t^n$. Build the discretized Lagrangian variable $(\rho^{\mathrm{Lag}}\mathbf{V}^{\mathrm{Lag}}, z^{\mathrm{Lag}}) = (\rho^n\mathbf{V}^n, z^n)$ associated with the discrete Eulerian variable$(\rho^n\mathbf{V}^n, z^n)$.

Step 2. Update the Lagrangian variable $(\rho^{\mathrm{Lag}}\mathbf{V}^{\mathrm{Lag}}, z^{\mathrm{Lag}})$ to the its state $(\tilde{\rho}\widetilde{\mathbf{V}}, \tilde{z})$ at instant $t=t^{n+1}$ by solving numerically system (6).

Step 3. Remap the Lagrangian variable $(\tilde{\rho}\widetilde{\mathbf{V}}, \tilde{z})$ onto the Eulerian mesh which provides the discretized Eulerian variable $(\rho^{n+1}\mathbf{V}^{n+1}, z^{n+1})$ at time $t=t^{n+1}$, by solving numerically system (5). This step accounts for the fact that the mesh associated with the Lagrangian system is deformed by (5) through the resolution of (6) from t^n to t^{n+1}.

As it will be shown in Section 3.4, a simple equation substitution allows to see that the overall algorithm can be put in conservative form for the variables $\rho, \rho y$, ρu and ρe.

For the sake of readability, we shall use the following notations: for $j \in \mathbb{Z}$ and $n \in \mathbb{N}$, we note

- q_j^n is an approximate value of the field q in the Eulerian frame within the cell j at instant t^n,
- $q_{j+1/2}$ is an approximate value of the field q in the Eulerian frame at the interface $j+1/2$ that separates the cell j and the cell $j+1$ at instant t^n,
- $\tilde{q}_j$ is an approximate value of the field q in the Lagrangian frame within the cell j at instant t^{n+1},
- $\tilde{q}_{j+1/2}$ is an approximate value of the field q in the Lagrangian frame at the interface $j+1/2$ that separates the cell j and the cell $j+1$ at instant t^{n+1}.

3.1.3. Lagrange step

The step 2 is a simple discretization of (6). Following [8] we use here the so-called "acoustic scheme" [5] that reads

$$\begin{cases} \tilde{y}_j = y_j^n, \\ \tilde{z}_j = z_j^n, \\ \rho_j^n \dfrac{\tilde{\tau}_j - \tau_j^n}{\Delta t} - \dfrac{1}{\Delta x}(u_{j+1/2} - u_{j-1/2}) = 0, \\ \rho_j^n \dfrac{\tilde{u}_j - u_j^n}{\Delta t} + \dfrac{1}{\Delta x}(P_{j+1/2} - P_{j-1/2}) = 0, \\ \rho_j^n \dfrac{\tilde{e}_j - e_j^n}{\Delta t} + \dfrac{1}{\Delta x}(P_{j+1/2}u_{j+1/2} - P_{j-1/2}u_{j-1/2}) = 0, \end{cases} \tag{7}$$

where the numerical fluxes are defined by

$$\begin{cases} u_{j+1/2} = \frac{1}{2}(u_{j+1}^n + u_j^n) - \frac{1}{2(\rho c)_{j+1/2}}(P_{j+1}^n - P_j^n), \\ P_{j+1/2} = \frac{1}{2}(P_{j+1}^n + P_j^n) - \frac{(\rho c)_{j+1/2}}{2}(u_{j+1}^n - u_j^n), \\ (\rho c)_{j+1/2} = \sqrt{\max\left[\rho_{j+1}^n (\mathbf{c}_{j+1}^n)^2, \rho_j (\mathbf{c}_j^n)^2\right] \min(\rho_{j+1}^n, \rho_j^n)}. \end{cases} \tag{8}$$

The time step Δt is chosen in agreement with the following Courant-Friedrichs-Lewy (CFL) condition:

$$\frac{\Delta t}{\Delta x} \max_{j \in \mathbb{Z}} \left(|u_{j+1/2}|, (\rho c)_{j+1/2} / \min\left(\rho_j^n, \rho_{j+1}^n\right)\right) \leqslant C^{\mathrm{CFL}} \tag{9}$$

with C^{CFL} usually chosen $C^{\mathrm{CFL}} \leqslant 0.8$. The stability of the Lagrange step (7) under the condition (9) has been investigated in [5].

3.1.4. Remap step

Let us now turn to the step 3. The procedure of remapping the Lagrangian variable onto the Eulerian mesh consists in a discrete resolution of system (5). Following classic lines (see [11]) we choose for this step a discretization of the form

$$\begin{cases} \dfrac{\rho_j^{n+1} - \rho_j^n}{\Delta t} + \dfrac{1}{\Delta x}(\tilde{\rho}_{j+1/2}u_{j+1/2} - \tilde{\rho}_{j-1/2}u_{j-1/2}) = 0, \\ \dfrac{\rho_j^{n+1}y_j^{n+1} - \rho_j^n \tilde{y}_j}{\Delta t} + \dfrac{1}{\Delta x}(\tilde{\rho}_{j+1/2}\tilde{y}_{j+1/2}u_{j+1/2} - \tilde{\rho}_{j-1/2}\tilde{y}_{j-1/2}u_{j-1/2}) = 0, \\ \dfrac{\rho_j^{n+1}u_j^{n+1} - \rho_j^n \tilde{u}_j}{\Delta t} + \dfrac{1}{\Delta x}(\tilde{\rho}_{j+1/2}\tilde{u}_{j+1/2}u_{j+1/2} - \tilde{\rho}_{j-1/2}\tilde{u}_{j-1/2}u_{j-1/2}) = 0, \\ \dfrac{\rho_j^{n+1}e_j^{n+1} - \rho_j^n \tilde{e}_j}{\Delta t} + \dfrac{1}{\Delta x}(\tilde{\rho}_{j+1/2}\tilde{e}_{j+1/2}u_{j+1/2} - \tilde{\rho}_{j-1/2}\tilde{e}_{j-1/2}u_{j-1/2}) = 0, \\ \dfrac{z_j^{n+1} - z_j^n}{\Delta t} + \dfrac{1}{\Delta x}(\tilde{z}_{j+1/2}u_{j+1/2} - \tilde{z}_{j-1/2}u_{j-1/2}) - \dfrac{1}{\Delta x}z_j^n(u_{j+1/2} - u_{j-1/2}) = 0. \end{cases} \tag{10}$$

The update (10) from $(\tilde{\rho}\widetilde{\mathbf{V}}, \tilde{z})$ to $(\rho^{n+1}\mathbf{V}^{n+1}, z^{n+1})$ is consistent with an advection step. Let us emphasize that (10) clearly shows a conservative discretization for the variables $\rho\mathbf{V}$ and a non-conservative discretization for z. Once again, the time step Δt is chosen according to the CFL condition (9), which ensures stability.

Given the Lagrange step described in Section 3.1.3 and given the framework (10) we only need to specify the numerical flux $(\tilde{\rho}\widetilde{\mathbf{V}}, \tilde{z})_{j+1/2}$ in order to obtain a totally defined Remap Step and therefore a totally defined Lagrange–Remap scheme. Consequently, building the numerical scheme boils down to define

$$\tilde{y}_{j+1/2}, \quad \tilde{\rho}_{j+1/2}, \quad \tilde{u}_{j+1/2}, \quad (\widetilde{\rho\varepsilon})_{j+1/2}, \quad \tilde{z}_{j+1/2}. \tag{11}$$

We propose to choose the quantities in (11) as follows: first, we enforce the flux consistency for y, ρ and ε by setting

$$\begin{aligned}
&\tilde{y}_{j+1/2} = \frac{\tilde{z}_{j+1/2}(\widetilde{\rho_1})_{j+1/2}}{\tilde{\rho}_{j+1/2}}, \\
&\tilde{\rho}_{j+1/2} = \tilde{z}_{j+1/2}(\widetilde{\rho_1})_{j+1/2} + (1-\tilde{z}_{j+1/2})(\widetilde{\rho_0})_{j+1/2}, \\
&\tilde{\rho}_{j+1/2}\tilde{\varepsilon}_{j+1/2} = \tilde{z}_{j+1/2}(\widetilde{\rho_1\varepsilon_1})_{j+1/2} + (1-\tilde{z}_{j+1/2})(\widetilde{\rho_0\varepsilon_0})_{j+1/2}.
\end{aligned} \tag{12}$$

The definition of the terms in (11) now boils down to choose the following fluxes:

$$(\widetilde{\rho_0})_{j+1/2}, \quad (\widetilde{\rho_1})_{j+1/2}, \quad (\widetilde{\rho_0\varepsilon_0})_{j+1/2}, \quad (\widetilde{\rho_1\varepsilon_1})_{j+1/2}, \quad \tilde{u}_{j+1/2}, \quad \tilde{z}_{j+1/2}.$$

For $(\widetilde{\rho_k})_{j+1/2}, (\widetilde{\rho_k\varepsilon_k})_{j+1/2}$ and $\tilde{u}_{j+1/2}$ we choose the upwind value according to the sign of the interface velocity $u_{j+1/2}$, namely

$$(\widetilde{\rho_0}, \widetilde{\rho_1}, \widetilde{\rho_0\varepsilon_0}, \widetilde{\rho_1\varepsilon_1}, \tilde{u})_{j+1/2} = \begin{cases} (\widetilde{\rho_0}, \widetilde{\rho_1}, \widetilde{\rho_0\varepsilon_0}, \widetilde{\rho_1\varepsilon_1}, \tilde{u})_j, & \text{if } u_{j+1/2} > 0, \\ (\widetilde{\rho_0}, \widetilde{\rho_1}, \widetilde{\rho_0\varepsilon_0}, \widetilde{\rho_1\varepsilon_1}, \tilde{u})_{j+1}, & \text{if } u_{j+1/2} < 0. \end{cases} \tag{13}$$

Finally, given the choices (13) and (12) the sole remaining problem consists in choosing the value of $\tilde{z}_{j+1/2}$. When we settle on this point, the construction of the numerical scheme will be completed. This task is the purpose of the next Sections 3.3.1, 3.3.2, 3.3.3, 3.3.4 and 3.2.

3.2. Choice of the flux $\tilde{z}_{j+1/2}$ and control of the numerical diffusion of the interface

For the sake of clarity we anticipate the results of the Section 3.3 and we propose in the present section some general guidelines inspired from the limited downwind strategy of [6,19,8]. These guidelines will allow us to choose $\tilde{z}_{j+1/2}$ so that the material interface remains sharp throughout the computation.

Let us suppose that we know a sequence of real intervals $(I_{j+1/2})_{j\in\mathbb{Z}}$ that shall be referred to as "trust intervals" in the sequel. These intervals are such that, for a given $j \in \mathbb{Z}$, if the flow variable $(\rho\mathbf{V}, z)^n$ matches a certain flow configuration $C_{j+1/2}$ in the neighboring cells of the interface $j+1/2$ then $\tilde{z}_{j+1/2} \in I_{j+1/2}$ implies that the scheme fulfills numerical features such as consistency and stability in some sense. Then we propose to choose $\tilde{z}_{j+1/2}$ according to the following strategy:

(a) If the flow $(\rho\mathbf{V}, z)^n$ does not match the flow configuration $C_{j+1/2}$ in a neighborhood of the interface $j+1/2$, then we choose $\tilde{z}_{j+1/2}$ as the upwind value of $z^n = \tilde{z}$ according to the sign of $u_{j+1/2}$.
(b) If the flow $(\rho\mathbf{V}, z)^n$ does match the flow configuration $C_{j+1/2}$ in a neighborhood of the interface $j+1/2$, then we choose $\tilde{z}_{j+1/2}$ such that it belongs to $I_{j+1/2}$ and such that $\tilde{z}_{j+1/2}$ is as close as possible to the downwind value of $\tilde{z} = z^n$ according to the sign of $u_{j+1/2}$.

This strategy means that when the trust interval $I_{j+1/2}$ provides stability and consistency, we choose for $\tilde{z}_{j+1/2}$ "the most downwind" possible value within $I_{j+1/2}$, when $I_{j+1/2}$ does not give any information about the choice of $\tilde{z}_{j+1/2}$ we choose the upwind value as a "safety measure".

In the sequel we shall see that the flow configurations $C_{j+1/2}$ we shall take into account simply relate to the sign of $u_{j+1/2}, u_{j-1/2}$ and $u_{j+3/2}$. Moreover, the next sections will allow us to build a trust interval $I_{j+1/2}$ that provides

- consistency for the flux $\tilde{z}_{j+1/2}$ (see Section 3.3.1),
- consistency for the flux $\tilde{y}_{j+1/2}$ (see Section 3.3.2),
- stability for variable z (see Section 3.3.3),
- stability for variable y (see Section 3.3.4).

Thanks to this list of features, although $\tilde{z}_{j+1/2}$ is chosen downwind or as close as possible to the downwind value, our scheme is endowed with good stability and consistency properties. This downwind choice constrained by stability and consistency will prevent the interface from being smeared by the numerical scheme as in [6,19,7,8].

Remark 4. For the special case of the one-dimensional scalar advection equation with constant velocity, it has been proven that the limited downwind strategy is equivalent to the Ultra-Bee limiter in the formalism developed by Sweby [55] or the Hyper-C scheme in the Normalized Variable Diagram of Leonard [44].

Sections 3.3.1, 3.3.2, 3.3.3 and 3.3.4 are dedicated to the detailed derivation of the trust intervals $I_{j+1/2}$ and the resulting overall algorithm is described in Section 3.4.

3.3. Trust interval for $\tilde{z}_{j+1/2}$

Before going any further we introduce the following notations:

$$m_{j+1/2} = \min\left(z_j^n, z_{j+1}^n\right), \quad M_{j+1/2} = \max\left(z_j^n, z_{j+1}^n\right),$$
$$\mathfrak{m}_{j+1/2} = \min\left(y_j^n, y_{j+1}^n\right), \quad \mathfrak{M}_{j+1/2} = \max\left(y_j^n, y_{j+1}^n\right).$$

We suppose that $0 \leqslant z_j^n \leqslant 1$ and $0 \leqslant y_j^n \leqslant 1$ for all $j \in \mathbb{Z}$, which implies that $m_{j+1/2}, M_{j+1/2}, \mathfrak{m}_{j+1/2}$ and $\mathfrak{M}_{j+1/2}$ belong to the interval $[0,1]$ for all $j \in \mathbb{Z}$. Moreover we make the assumption that

$$(\widetilde{\rho_0})_{j+1/2} > 0 \quad \text{and} \quad (\widetilde{\rho_1})_{j+1/2} > 0, \quad \forall j \in \mathbb{Z} \tag{14}$$

and that Δt and Δx satisfy the CFL condition (9).

3.3.1. Flux $\tilde{z}_{j+1/2}$ consistency constraint for $\tilde{z}_{j+1/2}$

As in [6,19,8] we remark that as soon as $m_{j+1/2} \leqslant \tilde{z}_{j+1/2} \leqslant M_{j+1/2}$ then the flux $\tilde{z}_{j+1/2}$ is consistent. Therefore there is a "trust interval" $[m_{j+1/2}, M_{j+1/2}]$ for $\tilde{z}_{j+1/2}$ that ensures the consistency of the flux for the variable z in the sense that

$$\tilde{z}_{j+1/2} \in [m_{j+1/2}, M_{j+1/2}] \Rightarrow \quad \text{consistency for } \tilde{z}_{j+1/2}. \tag{15}$$

In the following, we shall consider $\tilde{z}_{j+1/2} \in [m_{j+1/2}, M_{j+1/2}]$, for all $j \in \mathbb{Z}$.

3.3.2. Flux $\tilde{y}_{j+1/2}$ consistency constraint for $\tilde{z}_{j+1/2}$

Following similar lines as those of the previous section, we note that as soon as $\mathfrak{m}_{j+1/2} \leqslant \tilde{y}_{j+1/2} \leqslant \mathfrak{M}_{j+1/2}$ then the flux $\tilde{y}_{j+1/2}$ for the variable y is consistent. Using the definition (12), we see that $\mathfrak{m}_{j+1/2} \leqslant \tilde{y}_{j+1/2}$ is equivalent to

$$\mathfrak{m}_{j+1/2} \leqslant \frac{(\widetilde{\rho_1})_{j+1/2}\tilde{z}_{j+1/2}}{\tilde{z}_{j+1/2}(\widetilde{\rho_1})_{j+1/2} + (1-\tilde{z}_{j+1/2})(\widetilde{\rho_0})_{j+1/2}}, \tag{16}$$

which also reads

$$\tilde{z}_{j+1/2}\{(\widetilde{\rho_1})_{j+1/2}(1-\mathfrak{m}_{j+1/2}) + (\widetilde{\rho_0})_{j+1/2}\mathfrak{m}_{j+1/2}\} \geqslant (\widetilde{\rho_0})_{j+1/2}\mathfrak{m}_{j+1/2}.$$

According to the hypotheses presented at the beginning of Section 3.3, we see that $(\widetilde{\rho_1})_{j+1/2}(1-\mathfrak{m}_{j+1/2}) + (\widetilde{\rho_0})_{j+1/2}\mathfrak{m}_{j+1/2} > 0$ and therefore (16) is equivalent to

$$\frac{(\widetilde{\rho_0})_{j+1/2}\mathfrak{m}_{j+1/2}}{(\widetilde{\rho_1})_{j+1/2}(1-\mathfrak{m}_{j+1/2}) + (\widetilde{\rho_0})_{j+1/2}\mathfrak{m}_{j+1/2}} \leqslant \tilde{z}_{j+1/2}.$$

Using the same lines we see that an equivalent condition for $\tilde{z}_{j+1/2}$ to be such that $\tilde{y}_{j+1/2} \leqslant \mathfrak{M}_{j+1/2}$ is

$$\tilde{z}_{j+1/2} \leqslant \frac{(\widetilde{\rho_0})_{j+1/2}\mathfrak{M}_{j+1/2}}{(\widetilde{\rho_1})_{j+1/2}(1-\mathfrak{M}_{j+1/2}) + (\widetilde{\rho_0})_{j+1/2}\mathfrak{M}_{j+1/2}}.$$

Then if we note

$$d_{j+1/2} = \frac{(\widetilde{\rho_0})_{j+1/2}\mathfrak{m}_{j+1/2}}{(\widetilde{\rho_1})_{j+1/2}(1-\mathfrak{m}_{j+1/2}) + (\widetilde{\rho_0})_{j+1/2}\mathfrak{m}_{j+1/2}}, \tag{17}$$

$$D_{j+1/2} = \frac{(\widetilde{\rho_0})_{j+1/2}\mathfrak{M}_{j+1/2}}{(\widetilde{\rho_1})_{j+1/2}(1-\mathfrak{M}_{j+1/2}) + (\widetilde{\rho_0})_{j+1/2}\mathfrak{M}_{j+1/2}}, \tag{18}$$

we see that $[d_{j+1/2}, D_{j+1/2}]$ is a trust interval for $\tilde{z}_{j+1/2}$ that ensures consistency for the flux $\tilde{y}_{j+1/2}$ in the sense that

$$\tilde{z}_{j+1/2} \in [d_{j+1/2}, D_{j+1/2}] \Rightarrow \tilde{y}_{j+1/2} \in [\mathfrak{m}_{j+1/2}, \mathfrak{M}_{j+1/2}] \Rightarrow \text{consistency for } \tilde{y}_{j+1/2}.$$

In the sequel, we shall consider that $\tilde{z}_{j+1/2} \in [d_{j+1/2}, D_{j+1/2}]$, for all $j \in \mathbb{Z}$. We assume that this ansatz is compatible with $\tilde{z}_{j+1/2} \in [m_{j+1/2}, M_{j+1/2}]$, however, this point will be proven in Section 3.3.5.

3.3.3. Color function stability constraint for $\tilde{z}_{j+1/2}$

In the present section we shall exhibit a condition on $\tilde{z}_{j+1/2}$ that ensures stability for the variable z in a neighbor cell of the interface $j+1/2$ when the velocities at the interfaces of this cell have the same sign. More precisely, one considers the cell whose z value is "emptied" by the flux $\tilde{z}_{j+1/2}$, namely the cell j (resp. cell $j+1$) when $u_{j+1/2} > 0$ and $u_{j-1/2} > 0$ (resp. $u_{j+1/2} < 0$ and $u_{j+3/2} < 0$). Then we seek a sufficient condition that enforces a local maximum principle in the cell j (resp. cell $j+1$).

Suppose that $u_{j+1/2} > 0$ and $u_{j-1/2} > 0$. In this particular flow configuration for the cell j, we have a simple sufficient stability condition for z_j (see Fig. 2)

$$m_{j-1/2} \leqslant z_j^{n+1} \leqslant M_{j-1/2} \Rightarrow \text{stability for } z \text{ in the cell } j. \tag{19}$$

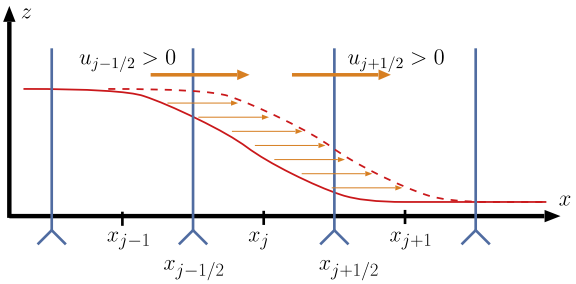

Fig. 2. Condition for the z-stability: for the configuration $u_{j+1/2} > 0$ and $u_{j-1/2} > 0$, the stability is ensured by $m_{j-1/2} \leqslant z_j^{n+1} \leqslant M_{j-1/2}$.

We shall now seek conditions on $\tilde{z}_{j+1/2}$ that ensure $z_j^{n+1} \in [m_{j-1/2}, M_{j-1/2}]$. According to (10), a sufficient condition for $m_{j-1/2} \leqslant z_j^{n+1}$ is given by

$$m_{j-1/2} \leqslant z_j^n - \frac{\Delta t}{\Delta x}(\tilde{z}_{j+1/2}u_{j+1/2} - \tilde{z}_{j-1/2}u_{j-1/2}) + \frac{\Delta t}{\Delta x} z_j^n (u_{j+1/2} - u_{j-1/2}),$$

which also reads

$$\frac{\Delta x}{\Delta t}\left(m_{j-1/2} - z_j^n\right) - z_j^n(u_{j+1/2} - u_{j-1/2}) - \tilde{z}_{j-1/2}u_{j-1/2} \leqslant -\tilde{z}_{j+1/2}u_{j+1/2}. \tag{20}$$

As $\tilde{z}_{j-1/2}$ is chosen within the consistency trust interval $[m_{j-1/2}, M_{j-1/2}]$, we have $-\tilde{z}_{j+1/2} \leqslant -m_{j-1/2}^n$. Consequently a sufficient condition for (20) to be satisfied is

$$\frac{\Delta x}{\Delta t}\left(m_{j-1/2} - z_j^n\right) - z_j^n(u_{j+1/2} - u_{j-1/2}) - m_{j-1/2}u_{j-1/2} \leqslant -\tilde{z}_{j+1/2}u_{j+1/2}$$

and equivalently

$$\tilde{z}_{j+1/2} \leqslant z_j^n + \left(m_{j-1/2} - z_j^n\right)\left(\frac{u_{j-1/2}}{u_{j+1/2}} - \frac{\Delta x}{\Delta t}\frac{1}{u_{j+1/2}}\right). \tag{21}$$

Symmetrically, we see that a sufficient condition for $\tilde{z}_{j+1/2}$ to imply $z_j^{n+1} \leqslant M_{j-1/2}$ is

$$z_j^n + \left(M_{j-1/2} - z_j^n\right)\left(\frac{u_{j-1/2}}{u_{j+1/2}} - \frac{\Delta x}{\Delta t}\frac{1}{u_{j+1/2}}\right) \leqslant \tilde{z}_{j+1/2}. \tag{22}$$

Finally if we note

$$\begin{cases} a_{j+1/2} = z_j^n + \left(M_{j-1/2} - z_j^n\right)\left(\dfrac{u_{j-1/2}}{u_{j+1/2}} - \dfrac{\Delta x}{\Delta t}\dfrac{1}{u_{j+1/2}}\right), \\ A_{j+1/2} = z_j^n + (m_{j-1/2} - z_j^n)\left(\dfrac{u_{j-1/2}}{u_{j+1/2}} - \dfrac{\Delta x}{\Delta t}\dfrac{1}{u_{j+1/2}}\right) \end{cases}$$

then we see that $[a_{j+1/2}, A_{j+1/2}]$ is a trust interval for $\tilde{z}_{j+1/2}$ that ensures the stability of z in the cell j when $u_{j+1/2} > 0$ and $u_{j-1/2} > 0$ in the sense that

$$\tilde{z}_{j+1/2} \in [a_{j+1/2}, A_{j+1/2}] \;\Rightarrow\; z_j^{n+1} \in [m_{j-1/2}, M_{j-1/2}] \;\Rightarrow\; \text{stability for } z \text{ in the cell } j.$$

By applying the same lines for the case $u_{j+1/2} < 0$ and $u_{j+3/2} < 0$, we obtain the following proposition.

Proposition 3.1. *Suppose that $\tilde{z}_{i+1/2}$ belongs to the consistency trust interval $[m_{i-1/2}, M_{i-1/2}]$, for all $i \in \mathbb{Z}$ and that the CFL condition (9) holds. We consider a given $j \in \mathbb{Z}$.*

(a) *If $u_{j+1/2} > 0$ and $u_{j+3/2} > 0$, we set*

$$\begin{cases} a_{j+1/2} = z_j^n + \left(M_{j-1/2} - z_j^n\right)\left(\dfrac{u_{j-1/2}}{u_{j+1/2}} - \dfrac{\Delta x}{\Delta t}\dfrac{1}{u_{j+1/2}}\right), \\ A_{j+1/2} = z_j^n + \left(m_{j-1/2} - z_j^n\right)\left(\dfrac{u_{j-1/2}}{u_{j+1/2}} - \dfrac{\Delta x}{\Delta t}\dfrac{1}{u_{j+1/2}}\right). \end{cases}$$

We have the following sufficient condition for local stability:

$$\tilde{z}_{j+1/2} \in [a_{j+1/2}, A_{j+1/2}] \;\Rightarrow\; z_j^{n+1} \in [m_{j-1/2}, M_{j-1/2}] \;\Rightarrow\; \textit{stability for } z \textit{ in the cell } j.$$

(b) *If $u_{j+1/2} < 0$ and $u_{j+3/2} < 0$, we set*

$$\begin{cases} a_{j+1/2} = z^n_{j+1} + \left(M_{j+3/2} - z^n_{j+1}\right)\left(\dfrac{u_{j+3/2}}{u_{j+1/2}} + \dfrac{\Delta x}{\Delta t}\dfrac{1}{u_{j+1/2}}\right), \\ A_{j+1/2} = z^n_{j+1} + \left(m_{j+3/2} - z^n_{j+1}\right)\left(\dfrac{u_{j+3/2}}{u_{j+1/2}} + \dfrac{\Delta x}{\Delta t}\dfrac{1}{u_{j+1/2}}\right). \end{cases}$$

Then we have the following sufficient condition for local stability:

$$\tilde{z}_{j+1/2} \in [a_{j+1/2}, A_{j+1/2}] \;\Rightarrow\; z^{n+1}_{j+1} \in [m_{j+3/2}, M_{j+3/2}] \;\Rightarrow\; \textit{stability for } z \textit{ in the cell } j+1.$$

Proposition 3.1 defines a trust interval for $\tilde{z}_{j+1/2}$ that ensures local stability for z: when $u_{j+1/2} > 0$ and $u_{j-1/2} > 0$, the stability condition deals with the value of z in the cell j, when $u_{j+1/2} < 0$ and $u_{j+3/2} < 0$, it deals with the value of z in the cell $j+1$.

3.3.4. Mass fraction stability constraint for $\tilde{z}_{j+1/2}$

According to Section 3.1.4, the mass fraction flux is given by $\tilde{y}_{j+1/2} = \tilde{z}_{j+1/2}\widetilde{(\rho_1)}_{j+1/2}/\tilde{\rho}_{j+1/2}$, where $\tilde{\rho}_{j+1/2} = \tilde{z}_{j+1/2}\widetilde{(\rho_1)}_{j+1/2} + (1-\tilde{z}_{j+1/2})\widetilde{(\rho_0)}_{j+1/2}$ and $\widetilde{(\rho_k)}_{j+1/2}, k = 0, 1$ are chosen using the upwind value by relation (13). We proceed following similar lines to those in Section 3.3.3: when $u_{j+1/2} > 0$ (resp. $u_{j+1/2} < 0$) we consider the neighboring cell j (resp. $j+1$) whose y value is "emptied" by the flux $y_{j+1/2}$. We consider a special flow pattern when $u_{j-1/2} > 0$ (resp. $u_{j+3/2} < 0$) and a condition on $\tilde{z}_{j+1/2}$ that guarantees a local maximum principle for y in the cell j (resp. cell $j+1$) through the definition of $\tilde{y}_{j+1/2}$.

We suppose that $u_{j+1/2} > 0$ and $u_{j-1/2} > 0$ and as in Section 3.3.3 for this particular flow configuration we see that we have the following stability condition for the value of y in the cell j

$$\mathfrak{m}_{j-1/2} \leqslant y^{n+1}_j \leqslant \mathfrak{M}_{j-1/2} \Rightarrow \text{ stability for } y \text{ in the cell } j.$$

We seek a sufficient condition that ensures

$$\mathfrak{m}_{j-1/2} \leqslant y^{n+1}_j. \tag{23}$$

By multiplying (23) by ρ^{n+1}_j and using (10) we see that (23) is equivalent to

$$\mathfrak{m}_{j-1/2}\left[\rho^n_j - \frac{\Delta t}{\Delta x}(\tilde{\rho}_{j+1/2}u_{j+1/2} - \tilde{\rho}_{j-1/2}u_{j-1/2})\right] \leqslant \rho^n_j y^n_j - \frac{\Delta t}{\Delta x}(\tilde{\rho}_{j+1/2}\tilde{y}_{j+1/2}u_{j+1/2} - \tilde{\rho}_{j-1/2}\tilde{y}_{j-1/2}u_{j-1/2}),$$

which also reads

$$\tilde{\rho}_{j+1/2}\tilde{y}_{j+1/2} \leqslant \frac{\Delta x}{\Delta t}\frac{\rho^n_j}{u_{j+1/2}}\left(y^n_j - \mathfrak{m}_{j-1/2}\right) + \frac{\tilde{\rho}_{j-1/2}u_{j-1/2}}{u_{j+1/2}}(\tilde{y}_{j-1/2} - \mathfrak{m}_{j-1/2}) + \mathfrak{m}_{j-1/2}\tilde{\rho}_{j+1/2}. \tag{24}$$

As we supposed $\tilde{z}_{j-1/2} \in [m_{j-1/2}, M_{j-1/2}]$ (see Section 3.3.1), therefore $\tilde{z}_{j-1/2} \in [0,1]$ and then using the assumption (14) we see that $\widetilde{\rho_{j-1/2}} \geqslant 0$. As we assumed the consistency constraint $\tilde{y}_{j+1/2} \in [\mathfrak{m}_{j-1/2}, \mathfrak{M}_{j-1/2}]$ to be verified (see Section 3.3.2), then we have $\frac{\tilde{\rho}_{j-1/2}u_{j-1/2}}{u_{j+1/2}}(\tilde{y}_{j-1/2} - \mathfrak{m}_{j-1/2}) \geqslant 0$. Thus we deduce that a sufficient condition for (24) and equivalently (23) to be true is

$$\tilde{\rho}_{j+1/2}\tilde{y}_{j+1/2} \leqslant \frac{\Delta x}{\Delta t}\frac{\rho^n_j}{u_{j+1/2}}\left(y^n_j - \mathfrak{m}_{j-1/2}\right) + \mathfrak{m}_{j-1/2}\tilde{\rho}_{j+1/2}. \tag{25}$$

The inequality (25) is not an explicit constraint upon $\tilde{z}_{j+1/2}$ therefore we need to investigate a little further. We use the definition (12) for $\tilde{\rho}_{j+1/2}\tilde{y}_{j+1/2}$ and $\tilde{\rho}_{j+1/2}$ in (25) and as $\widetilde{(\rho_k)}_{j+1/2} = \widetilde{(\rho_k)}_j, k = 0, 1$ according to the upwind choice (13) we find that (25) is equivalent to

$$\left[\widetilde{(\rho_0)}_j\mathfrak{m}_{j-1/2} + \widetilde{(\rho_1)}_j(1-\mathfrak{m}_{j-1/2})\right]\tilde{z}_{j+1/2} \leqslant \frac{\Delta x}{\Delta t}\frac{\rho^n_j}{u_{j+1/2}}\left(y^n_j - \mathfrak{m}_{j-1/2}\right) + \widetilde{(\rho_0)}_j\mathfrak{m}_{j-1/2}. \tag{26}$$

As $\mathfrak{m}_{j-1/2} \in [0,1]$, we see that $\widetilde{(\rho_0)}_j\mathfrak{m}_{j-1/2} + \widetilde{(\rho_1)}_j(1-\mathfrak{m}_{j-1/2}) \geqslant 0$ and therefore that inequality (26) gives indeed an upper bound for $\tilde{z}_{j+1/2}$. Moreover, we notice that this bound is explicit as it only involves terms whose definition does not rely on $\tilde{z}_{j+1/2}$. For the sake of consistency with the formula of Proposition 3.1 we propose the following equivalent bound: let us divide the relation (26) by $\tilde{\rho}_j$ then by noticing

$$\frac{\widetilde{(\rho_k)}}{\tilde{\rho}_j} = \frac{\widetilde{(y_k)_j}}{\widetilde{(z_k)_j}} = \frac{(y_k)^n_j}{(z_k)^n_j} = \frac{(\rho_k)^n_j}{\rho^n_j}, \quad k = 0, 1$$

and by using the expression of $\rho^n_j/\tilde{\rho}_j$ given by (7) we find that (26) reads

$$\tilde{z}_{j+1/2} \leqslant z^n_j + \frac{\rho^n_j\left(\mathfrak{m}_{j-1/2} - y^n_j\right)}{(\rho_0)^n_j\mathfrak{m}_{j-1/2} + (\rho_1)^n_j(1-\mathfrak{m}_{j-1/2})}\left(\frac{u_{j-1/2}}{u_{j+1/2}} - \frac{\Delta x}{\Delta t}\frac{1}{u_{j+1/2}}\right).$$

Symmetrically, a sufficient condition for $\tilde{z}_{j+1/2}$ to be such that $y_j^{n+1} \leqslant \mathfrak{M}_{j-1/2}$ is provided by

$$z_j^n + \frac{\rho_j^n\left(\mathfrak{M}_{j-1/2} - y_j^n\right)}{(\rho_0)_j^n \mathfrak{M}_{j-1/2} + (\rho_1)_j^n(1-\mathfrak{M}_{j-1/2})}\left(\frac{u_{j-1/2}}{u_{j+1/2}} - \frac{\Delta x}{\Delta t}\frac{1}{u_{j+1/2}}\right) \leqslant \tilde{z}_{j+1/2}.$$

Finally if we note

$$\begin{cases} b_{j+1/2} = z_j^n + \dfrac{\rho_j^n\left(\mathfrak{M}_{j-1/2} - y_j^n\right)}{(\rho_0)_j^n \mathfrak{M}_{j-1/2} + (\rho_1)_j^n(1-\mathfrak{M}_{j-1/2})}\left(\dfrac{u_{j-1/2}}{u_{j+1/2}} - \dfrac{\Delta x}{\Delta t}\dfrac{1}{u_{j+1/2}}\right), \\ B_{j+1/2} = z_j^n + \dfrac{\rho_j^n\left(\mathfrak{m}_{j-1/2} - y_j^n\right)}{(\rho_0)_j^n \mathfrak{m}_{j-1/2} + (\rho_1)_j^n(1-\mathfrak{m}_{j-1/2})}\left(\dfrac{u_{j-1/2}}{u_{j+1/2}} - \dfrac{\Delta x}{\Delta t}\dfrac{1}{u_{j+1/2}}\right), \end{cases}$$

we see that $[b_{j+1/2}, B_{j+1/2}]$ is a "trust interval" for choosing a value of $\tilde{z}_{j+1/2}$ that ensures a local stability for y in the cell j when $u_{j+1/2} > 0$ and $u_{j-1/2} > 0$ in the following sense:

$$\tilde{z}_{j+1/2} \in [b_{j+1/2}, B_{j+1/2}] \;\Rightarrow\; y_j^{n+1} \in [\mathfrak{m}_{j-1/2}, \mathfrak{M}_{j-1/2}] \;\Rightarrow\; \text{stability for } y \text{ in the cell } j.$$

We can perform a similar analysis for the case $u_{j+1/2} < 0$ and $u_{j+3/2} < 0$ and finally we obtain the following proposition.

Proposition 3.2. *Suppose that $\tilde{z}_{i+1/2} \in [m_{i-1/2}, M_{i-1/2}]$ and suppose that $\tilde{y}_{i+1/2} \in [\mathfrak{m}_{i-1/2}, \mathfrak{M}_{i-1/2}]$, for all $i \in \mathbb{Z}$ and that the CFL condition (9) holds. Consider a given $j \in \mathbb{Z}$.*

(a) *If $u_{j+1/2} > 0$ and $u_{j-1/2} > 0$ then we set*

$$\begin{cases} b_{j+1/2} = z_j^n + \dfrac{\rho_j^n\left(\mathfrak{M}_{j-1/2} - y_j^n\right)}{(\rho_0)_j^n \mathfrak{M}_{j-1/2} + (\rho_1)_j^n(1-\mathfrak{M}_{j-1/2})}\left(\dfrac{u_{j-1/2}}{u_{j+1/2}} - \dfrac{\Delta x}{\Delta t}\dfrac{1}{u_{j+1/2}}\right), \\ B_{j+1/2} = z_j^n + \dfrac{\rho_j^n\left(\mathfrak{m}_{j-1/2} - y_j^n\right)}{(\rho_0)_j^n \mathfrak{m}_{j-1/2} + (\rho_1)_j^n(1-\mathfrak{m}_{j-1/2})}\left(\dfrac{u_{j-1/2}}{u_{j+1/2}} - \dfrac{\Delta x}{\Delta t}\dfrac{1}{u_{j+1/2}}\right). \end{cases}$$

We have the following sufficient condition for local stability:

$$\tilde{z}_{j+1/2} \in [b_{j+1/2}, B_{j+1/2}] \;\Rightarrow\; y_j^{n+1} \in [\mathfrak{m}_{j-1/2}, \mathfrak{M}_{j-1/2}] \;\Rightarrow\; \text{stability for } y \text{ in the cell } j.$$

(b) *If $u_{j+1/2} < 0$ and $u_{j+3/2} < 0$ then we set*

$$\begin{cases} b_{j+1/2} = z_{j+1}^n + \dfrac{\rho_{j+1}^n\left(\mathfrak{M}_{j+3/2} - y_{j+1}^n\right)}{(\rho_0)_{j+1}^n \mathfrak{M}_{j+3/2} + (\rho_1)_{j+1}^n(1-\mathfrak{M}_{j+3/2})}\left(\dfrac{u_{j+3/2}}{u_{j+1/2}} + \dfrac{\Delta x}{\Delta t}\dfrac{1}{u_{j+1/2}}\right), \\ B_{j+1/2} = z_{j+1}^n + \dfrac{\rho_{j+1}^n\left(\mathfrak{m}_{j+3/2} - y_{j+1}^n\right)}{(\rho_0)_{j+1}^n \mathfrak{m}_{j+3/2} + (\rho_1)_{j+1}^n(1-\mathfrak{m}_{j+3/2})}\left(\dfrac{u_{j+3/2}}{u_{j+1/2}} + \dfrac{\Delta x}{\Delta t}\dfrac{1}{u_{j+1/2}}\right). \end{cases}$$

We have the following sufficient condition for local stability:

$$\tilde{z}_{j+1/2} \in [b_{j+1/2}, B_{j+1/2}] \;\Rightarrow\; y_{j+1}^{n+1} \in [\mathfrak{m}_{j+3/2}, \mathfrak{M}_{j+3/2}] \;\Rightarrow\; \text{stability for } y \text{ in the cell } j+1.$$

3.3.5. Existence of the trust interval

In the previous sections we exhibited several "trust intervals" that, respectively, ensure consistency for the flux $\tilde{z}_{j+1/2}$ (see Section 3.3.1), consistency for the flux $\tilde{y}_{j+1/2}$ (see Section 3.3.2), stability for the variable z (see Section 3.3.3) and stability for the variable y (see Section 3.3.4). Let us first remark that we did not rule out the fact that some of these intervals may be empty. Moreover, as we wish to impose all of these features we need to consider a trust interval $I_{j+1/2}$ that intersects all of the previously mentioned intervals, namely

$$I_{j+1/2} = [m_{j+1/2}, M_{j+1/2}] \cap [d_{j+1/2}, D_{j+1/2}] \cap [a_{j+1/2}, A_{j+1/2}] \cap [b_{j+1/2}, B_{j+1/2}]. \tag{27}$$

Consequently, we also need to check that $I_{j+1/2} \neq \emptyset$. The answer to both questions lies in the fact that the upwind (according to the sign of $u_{j+1/2}$) value for $\tilde{z}_{j+1/2}$ belongs to each of the previous intervals. Indeed we have the following result.

Proposition 3.3. *Let $j \in \mathbb{Z}$, let us define $I_{j+1/2}$ according to relation (27).*

(a) *If $u_{j+1/2} > 0$ and $u_{j-1/2} > 0$, then $z_j^n \in I_{j+1/2} \neq \emptyset$.*
(b) *If $u_{j+1/2} < 0$ and $u_{j+3/2} < 0$, then $z_{j+1}^n \in I_{j+1/2} \neq \emptyset$.*

Proof. Let us suppose $u_{j+1/2} > 0$ and $u_{j-1/2} > 0$. In this case we need to show that

$$\tilde{z}_j = z_j^n \in [m_{j+1/2}, M_{j+1/2}] \cap [d_{j+1/2}, D_{j+1/2}] \cap [a_{j+1/2}, A_{j+1/2}] \cap [b_{j+1/2}, B_{j+1/2}].$$

First we see that

$$m_{j+1/2} = \min\left(z_j^n, z_{j+1}^n,\right) \leqslant z_j^n.$$

Then by using the consistency of the flux $\tilde{y}_{j+1/2}$, the upwind choice (13) provides in our case that

$$\widetilde{(\rho_1)}_{j+1/2} = \widetilde{(\rho_1)}_j = \tilde{\rho}_j \frac{\tilde{y}_j}{\tilde{z}_j} = \tilde{\rho}_j \frac{y_j^n}{z_j^n} \quad \text{and} \quad \widetilde{(\rho_0)}_{j+1/2} = \widetilde{(\rho_0)}_j = \tilde{\rho}_j \frac{1-\tilde{y}_j}{1-\tilde{z}_j} = \tilde{\rho}_j \frac{1-y_j^n}{1-z_j^n}.$$

According to the definition (17) we have

$$d_{j+1/2} = \frac{\mathfrak{m}_{j+1/2} \frac{1-y_j^n}{1-z_j^n}}{(1-\mathfrak{m}_{j+1/2}) \frac{y_j^n}{z_j^n} + \mathfrak{m}_{j+1/2} \frac{1-y_j^n}{1-z_j^n}}.$$

Therefore

$$d_{j+1/2} - z_j^n = -\frac{z_j^n(1-z_j^n)(y_j^n - \mathfrak{m}_{j+1/2})}{(1-\mathfrak{m}_{j+1/2}) y_j^n \left(1-z_j^n\right) + \mathfrak{m}_{j+1/2}\left(1-y_j^n\right) z_j^n}.$$

As $\mathfrak{m}_{j+1/2}, z_j^n$ and y_j^n belong to $[0,1]$ and as by definition $\mathfrak{m}_{j+1/2} = \min(y_j^n, y_{j+1}^n) \leqslant y_j^n$, we deduce that

$$d_{j+1/2} \leqslant z_j^n.$$

With the definitions in Proposition 3.1

$$a_{j+1/2} = z_j^n - \frac{(M_{j-1/2} - z_j^n)}{u_{j+1/2}} \frac{\Delta x}{\Delta t}\left(1 - \frac{\Delta t}{\Delta x} u_{j-1/2}\right).$$

As by definition $M_{j-1/2} = \max\left(z_{j-1}^n, z_j^n\right) \leqslant z_j^n$ and as the CFL condition (9) imposes that $u_{j-1/2}\frac{\Delta t}{\Delta x} \leqslant 1$, we deduce that

$$a_{j+1/2} \leqslant z_j^n.$$

For the constraint of stability for the variable y, according to the definitions given in Proposition 3.2

$$b_{j+1/2} = z_j^n - \frac{\rho_j^n \frac{\Delta x}{\Delta t} \frac{\mathfrak{M}_{j-1/2} - y_j^n}{u_{j+1/2}}}{(\rho_0)_j^n \mathfrak{M}_{j-1/2} + (\rho_1)_j^n (1-\mathfrak{M}_{j-1/2})}\left(1 - \frac{\Delta t}{\Delta x} u_{j-1/2}\right).$$

We know that $\mathfrak{M}_{j-1/2} = \max\left(y_{j-1}^n, y_j^n\right) \geqslant y_j^n$ and that $\mathfrak{M}_{j-1/2} \in [0,1]$, altogether with the positivity hypothesis (14) and the CFL condition (9), we obtain that

$$b_{j+1/2} \leqslant z_j^n.$$

Using similar lines we also obtain that $z_j^n \leqslant M_{j+1/2}, z_j^n \leqslant D_{j+1/2}, z_j^n \leqslant A_{j+1/2}$ and $z_j^n \leqslant B_{j+1/2}$, which proves the point (a). The point (b) can be proven using the same arguments. □

3.4. Overall algorithm

Let us first verify that the anti-diffusive numerical scheme is conservative with respect to the variables $\rho y, \rho, \rho u$ and ρe. Indeed, using the relations (7) and (10) the overall numerical scheme reads

$$\begin{cases}
\dfrac{\rho_j^{n+1} y_j^{n+1} - \rho_j^n y_j^n}{\Delta t} + \dfrac{1}{\Delta x}\left(\tilde{\rho}_{j+1/2}\tilde{y}_{j+1/2} u_{j+1/2} - \tilde{\rho}_{j-1/2}\tilde{y}_{j-1/2} u_{j-1/2}\right) = 0, \\
\dfrac{\rho_j^{n+1} - \rho_j^n}{\Delta t} + \dfrac{1}{\Delta x}\left(\tilde{\rho}_{j+1/2} u_{j+1/2} - \tilde{\rho}_{j-1/2} u_{j-1/2}\right) = 0, \\
\dfrac{\rho_j^{n+1} u_j^{n+1} - \rho_j^n u_j^n}{\Delta t} + \dfrac{1}{\Delta x}\left(\tilde{\rho}_{j+1/2}\tilde{u}_{j+1/2} u_{j+1/2} + P_{j+1/2} - \tilde{\rho}_{j-1/2}\tilde{u}_{j-1/2} u_{j-1/2} - P_{j-1/2}\right) = 0, \\
\dfrac{\rho_j^{n+1} e_j^{n+1} - \rho_j^n e_j^n}{\Delta t} + \dfrac{1}{\Delta x}\left(\tilde{\rho}_{j+1/2}\tilde{e}_{j+1/2} u_{j+1/2} + P_{j+1/2} u_{j+1/2} - \tilde{\rho}_{j-1/2}\tilde{e}_{j-1/2} u_{j-1/2} - P_{j-1/2} u_{j-1/2}\right) = 0, \\
\dfrac{z_j^{n+1} - z_j^n}{\Delta t} + \dfrac{1}{\Delta x}\left(\tilde{z}_{j+1/2} u_{j+1/2} - \tilde{z}_{j-1/2} u_{j-1/2}\right) - \dfrac{1}{\Delta x} z_j^n (u_{j+1/2} - u_{j-1/2}) = 0.
\end{cases}$$

The scheme is composed of a conservative part for $\rho\mathbf{V} = [\rho y, \rho, \rho u, \rho e]^T$ and an advection-type discretization for z which shows that our algorithm is quasi-conservative as the algorithm presented in [2,3].

We now give a step-by-step view of the full anti-diffusive algorithm.

1. For each cell interface $j+1/2$, compute $u_{j+1/2}, (\rho c)_{j+1/2}$ and $P_{j+1/2}$.
2. Compute Δt in agreement with the CFL constraint (9).
3. Compute $(\tilde{\rho}\tilde{\mathbf{V}}, \tilde{z})_j$ according to (7) for all j.
4. For each cell interface $j+1/2$, compute the numerical flux $\tilde{z}_{j+1/2}$ as follows:
   - if $u_{j+1/2} > 0$
     - if $u_{j-1/2} > 0$, compute the bounds of the trust interval $I_{j+1/2} = [\omega_{j+1/2}, \Omega_{j+1/2}]$ defined by (27), then
     $$\begin{cases} \text{if } z^n_{j+1} \leqslant \omega_{j+1/2}, & \text{then choose } \tilde{z}_{j+1/2} = \omega_{j+1/2}, \\ \text{if } \omega_{j+1/2} < z^n_{j+1} < \Omega_{j+1/2}, & \text{then choose } \tilde{z}_{j+1/2} = z^n_{j+1}, \\ \text{if } \Omega_{j+1/2} \leqslant z^n_{j+1}, & \text{then choose } \tilde{z}_{j+1/2} = \Omega_{j+1/2}. \end{cases}$$
     - if $u_{j-1/2} < 0$, choose the upwind value
     $$\tilde{z}_{j+1/2} = z^n_j.$$
   - if $u_{j+1/2} < 0$
     - if $u_{j+3/2} > 0$, choose the upwind value
     $$\tilde{z}_{j+1/2} = z^n_{j+1}.$$
     - if $u_{j+3/2} < 0$, compute the bounds of the trust interval $I_{j+1/2} = [\omega_{j+1/2}, \Omega_{j+1/2}]$ defined by (27), then
     $$\begin{cases} \text{if } z^n_j \leqslant \omega_{j+1/2}, & \text{then choose } \tilde{z}_{j+1/2} = \omega_{j+1/2}, \\ \text{if } \omega_{j+1/2} < z^n_j < \Omega_{j+1/2}, & \text{then choose } \tilde{z}_{j+1/2} = z^n_j, \\ \text{if } \Omega_{j+1/2} \leqslant z^n_{j+1}, & \text{then choose } \tilde{z}_{j+1/2} = \Omega_{j+1/2}. \end{cases}$$
5. For each cell interface $j+1/2$, compute the interface values $\tilde{y}_{j+1/2}, \tilde{\rho}_{j+1/2}, (\widetilde{\rho\varepsilon})_{j+1/2}$ and $\tilde{u}_{j+1/2}$, according to (12) and (13).
6. Update $(\tilde{\rho}\tilde{\mathbf{V}}, \tilde{z})_j$ into $(\rho\mathbf{V}, z)^{n+1}_j$ using (10) for all j.

4. Evolution of constant pressure and velocity profiles

A classic issue for the simulation of compressible flows involving two-component interfaces lies in ensuring that the numerical scheme will not develop spurious oscillations at the material interface. Indeed, although the pressure and the velocity are Riemann invariants for the contact discontinuity associated with the material interface of the five-equation model [2,3], when the interface is smeared by the discretization, inconsistencies may appear between the extended EOS, the state variable $(\rho\mathbf{V}, z)$ and the pressure P. This question has been examined by several authors for the past years within the framework of various multi-component models [16,17,1,32,28,27,33,2,34,20,3,58,21,8].

For the five-equation model with isobaric closure, the Roe-type scheme [26] presented in [2,3] provides a good discretization of the Riemann invariants across the material interface in the sense that it preserves some constant pressure and velocity profiles for a wide range of EOSs. Proposition 4.1 shows that the anti-diffusive scheme is endowed with a similar property.

Proposition 4.1. *Let $(\rho^n\mathbf{V}^n, z^n)$ be the approximate state variable at instant $t^n = n\Delta t$ computed with the anti-diffusive scheme. Suppose that $(\rho^n\mathbf{V}^n, z^n)$ is a contact discontinuity with uniform velocity and pressure such that for all $j \in \mathbb{Z}$ we have*

$$P^n_j = \overline{P}, \qquad u^n_j = \bar{u}, \tag{28}$$
$$(\rho_0)^n_j = \overline{\rho_0}, \quad (\rho_1)^n_j = \overline{\rho_1}, \tag{29}$$

where $\overline{P}, \bar{u}, \overline{\rho_0}, \overline{\rho_1}$ are constants. Then, the approximate state variable $(\rho^{n+1}\mathbf{V}^{n+1}, z^{n+1})$ computed with the anti-diffusive scheme verifies

$$P^{n+1}_j = \overline{P}, \qquad u^{n+1}_j = \bar{u}, \quad \forall j \in \mathbb{Z}, \tag{30}$$
$$(\rho_0)^{n+1}_j = \overline{\rho_0}, \quad (\rho_1)^{n+1}_j = \overline{\rho_1}, \quad \forall j \in \mathbb{Z}. \tag{31}$$

Proof. We use thereafter the same notations as in Section 3. We suppose here without loss of generality that $\bar{u} > 0$. Before going any further, let us remark that as the pressure and both phasic densities are uniform at time t^n, then both phasic internal energies at time t^n are also uniform. Indeed, using the pure fluid state laws $(\rho_k, P_k) \mapsto \rho_k\varepsilon_k(\rho_k, P_k)$, one can set

$$\forall j \in \mathbb{Z}, \quad (\rho_k\varepsilon_k)^n_j = (\rho_k\varepsilon_k)(\overline{\rho_k}, \overline{P}) = \overline{\rho_k\varepsilon_k}.$$

Let us examine the Lagrangian approximate solution obtained after the Lagrange step (7). As pressure and velocity are uniform, the fluxes for the Lagrange step defined by relations (8) read

$$u_{j+1/2} = \bar{u}, \quad P_{j+1/2} = \overline{P}, \quad \forall j \in \mathbb{Z}.$$

After the Lagrange step defined by relations (7) and (8) we obtain for all $j \in \mathbb{Z}$

$$\tilde{z}_j = z_j^n, \quad \tilde{y}_j = y_j^n, \quad \tilde{\tau}_j = \tau_j^n, \quad \tilde{u}_j = u_j^n = \bar{u}, \quad \tilde{e}_j = e_j^n.$$

First we deduce that

$$\widetilde{(\rho_k)}_j = \frac{\widetilde{(y_k)_j}}{\tilde{\tau}_j \widetilde{(z_k)}_j} = \frac{(y_k)_j^n}{\tau_j^n (z_k)_j^n} = (\rho_k)_j^n = \overline{\rho_k}, \quad k = 0, 1.$$

We also have $\tilde{\varepsilon}_j = \varepsilon_j^n$ and thus $\widetilde{(\rho\varepsilon)}_j = (\rho\varepsilon)_j^n$. The pressure $\widetilde{P}_j$ and the phasic energies $\widetilde{(\rho_k\varepsilon_k)}_j, k = 0, 1$ associated with the updated Lagrangian state $(\widetilde{\rho_j \mathbf{V}_j}, \tilde{z}_j)$ verify relations (2), which read here

$$\begin{cases} \widetilde{P}_j = P_0(\overline{\rho_0}, \widetilde{(\rho_0\varepsilon_0)}_j) = P_1(\overline{\rho_1}, \widetilde{(\rho_1\varepsilon_1)}_j), \\ \widetilde{(\rho\varepsilon)}_j = (\rho\varepsilon)_j^n = z_j^n \widetilde{(\rho_1\varepsilon_1)}_j + (1 - z_j^n)\widetilde{(\rho_0\varepsilon_0)}_j. \end{cases} \tag{32}$$

However, we know that the pressure $P_j^n = \overline{P}$ and the phasic energies $(\rho_k\varepsilon_k)_j^n = \overline{\rho_k\varepsilon_k}, k = 0, 1$ associated with the state variable $(\rho_j^n \mathbf{V}_j^n, z_j^n)$ at time t^n verify relations (2), namely

$$\begin{cases} \overline{P} = P_0(\overline{\rho_0}, \overline{\rho_0\varepsilon_0}) = P_1(\overline{\rho_1}, \overline{\rho_1\varepsilon_1}), \\ (\rho\varepsilon)_j^n = z_j^n \overline{\rho_1\varepsilon_1} + (1 - z_j^n)\overline{\rho_0\varepsilon_0}. \end{cases} \tag{33}$$

We see then that $(\widetilde{P}_j, \widetilde{(\rho_0\varepsilon_0)}_j, \widetilde{(\rho_1\varepsilon_1)}_j)$ and $(\overline{P}, \overline{\rho_0\varepsilon_0}, \overline{\rho_1\varepsilon_1})$ are, respectively, solutions of (32) and (33), which are the same system. According to the hypotheses of Section 2, the isobaric closure system (2) admits a unique solution. Therefore

$$\widetilde{P}_j = \overline{P}, \quad \widetilde{(\rho_0\varepsilon_0)}_j = \overline{\rho_0\varepsilon_0}, \quad \widetilde{(\rho_1\varepsilon_1)}_j = \overline{\rho_1\varepsilon_1}, \quad \forall j \in \mathbb{Z}.$$

We shall now consider the Remap step (10). In our case we have

$$\rho_j^{n+1} - \rho_j^n + \frac{\Delta t}{\Delta x}\bar{u}(\tilde{\rho}_{j+1/2} - \tilde{\rho}_{j-1/2}) = 0, \tag{34}$$

$$\rho_j^{n+1} y_j^{n+1} - \rho_j^n y_j^n + \frac{\Delta t}{\Delta x}\bar{u}(\tilde{\rho}_{j+1/2}\tilde{y}_{j+1/2} - \tilde{\rho}_{j-1/2}\tilde{y}_{j-1/2}) = 0, \tag{35}$$

$$\rho_j^{n+1} u_j^{n+1} - \rho_j^n \bar{u} + \frac{\Delta t}{\Delta x}\bar{u}(\tilde{\rho}_{j+1/2}\tilde{u}_{j+1/2} - \tilde{\rho}_{j-1/2}\tilde{u}_{j-1/2}) = 0, \tag{36}$$

$$\rho_j^{n+1} e_j^{n+1} - \rho_j^n \tilde{e}_j + \frac{\Delta t}{\Delta x}\bar{u}(\tilde{\rho}_{j+1/2}\tilde{e}_{j+1/2} - \tilde{\rho}_{j-1/2}\tilde{e}_{j-1/2}) = 0, \tag{37}$$

$$z_j^{n+1} - z_j^n + \frac{\Delta t}{\Delta x}\bar{u}(\tilde{z}_{j+1/2} - \tilde{z}_{j-1/2}) = 0. \tag{38}$$

As we supposed $\bar{u} > 0$, the upwind cell relatively to the interface $j + 1/2$ is the cell j. Therefore, we have for all $j \in \mathbb{Z}$

$$\begin{aligned} \widetilde{(\rho_1)}_{j+1/2} &= \widetilde{(\rho_1)}_j = \overline{\rho_1}, & \widetilde{(\rho_2)}_{j+1/2} &= \widetilde{(\rho_2)}_j = \overline{\rho_2}, \\ \widetilde{(\rho_1\varepsilon_1)}_{j+1/2} &= \widetilde{(\rho_1\varepsilon_1)}_j = \overline{\rho_1\varepsilon_1}, & \widetilde{(\rho_2\varepsilon_2)}_{j+1/2} &= \widetilde{(\rho_2\varepsilon_2)}_j = \overline{\rho_2\varepsilon_2}, \\ \tilde{u}_{j+1/2} &= \tilde{u}_j = \bar{u}. \end{aligned}$$

Then, injecting relation (34) into (36) provides $\rho_j^{n+1}(u_j^{n+1} - \bar{u}) = 0$. If we suppose that there is no vacuum formation in the computational domain, namely $\rho_j^{n+1} > 0$ for all $j \in \mathbb{Z}$, we obtain

$$u_j^{n+1} = \bar{u}, \quad \forall j \in \mathbb{Z}.$$

As a consequence, all the terms related to the kinetic energy vanish in relation (37), which gives

$$\begin{aligned} \rho_j^{n+1}\varepsilon_j^{n+1} &= \rho_j^n \tilde{\varepsilon}_j - \frac{\Delta t}{\Delta x}\bar{u}(\tilde{\rho}_{j+1/2}\tilde{\varepsilon}_{j+1/2} - \tilde{\rho}_{j-1/2}\tilde{\varepsilon}_{j-1/2}) = \sum_{k=0,1}(z_k)_j^n \overline{\rho_k\varepsilon_k} - \frac{\Delta t}{\Delta x}\bar{u}\left[\sum_{k=0,1}\widetilde{(z_k)}_{j+1/2}\overline{\rho_k\varepsilon_k} - \sum_{k=0,1}\widetilde{(z_k)}_{j-1/2}\overline{\rho_k\varepsilon_k}\right] \\ &= \sum_{k=0,1}\overline{\rho_k\varepsilon_k}\left[(z_k)_j^n - \frac{\Delta t}{\Delta x}\bar{u}\left(\widetilde{(z_k)}_{j+1/2} - \widetilde{(z_k)}_{j-1/2}\right)\right]. \end{aligned}$$

Thanks to relation (38) we obtain

$$\rho_j^{n+1}\varepsilon_j^{n+1} = z_j^{n+1}\overline{\rho_1\varepsilon_1} + (1 - z_j^{n+1})\overline{\rho_0\varepsilon_0}. \tag{39}$$

By considering the mass fraction remap provided by relation (35) and the fluxes definition (12) we find that

$$z_j^{n+1}(\rho_1)_j^{n+1} - z_j^n\overline{\rho_1} + \frac{\Delta t}{\Delta x}\bar{u}\overline{\rho_1}[\tilde{z}_{j+1/2} - \tilde{z}_{j-1/2}].$$

Therefore, we have $z_j^{n+1}[(\rho_1)_j^{n+1} - \overline{\rho_1}] = 0$, which implies that for all $j \in \mathbb{Z}$

$$(\rho_1)_j^{n+1} = \overline{\rho_1} \quad \text{and similarly} \quad (\rho_0)_j^{n+1} = \overline{\rho_0}.$$

The pressure P_j^{n+1} is thus solution of the system

$$\begin{cases} P_1\left(\overline{\rho_1}, (\rho_1\varepsilon_1)_j^{n+1}\right) = P_0\left(\overline{\rho_0}, (\rho_0\varepsilon_0)_j^{n+1}\right), \\ (\rho\varepsilon)_j^{n+1} = z_j^{n+1}(\rho_1\varepsilon_1)_j^{n+1} + (1 - z_j^{n+1})(\rho_0\varepsilon_0)_j^{n+1}. \end{cases} \tag{40}$$

However, thanks to relation (39) we can see that a possible solution for (40) reads

$$(\rho_1\varepsilon_1)_j^{n+1} = \overline{\rho_1\varepsilon_1}, \quad (\rho_0\varepsilon_0)_j^{n+1} = \overline{\rho_0\varepsilon_0}, \quad P_j^{n+1} = P_1(\overline{\rho_1}, \overline{\rho_1\varepsilon_1}) = P_0(\overline{\rho_0}, \overline{\rho_0\varepsilon_0}) = \overline{P}.$$

According to the hypotheses of Section 2 regarding the isobaric closure system, we know that this solution is unique and finally, we can conclude that $P_j^{n+1} = \overline{P}$. □

Remark 5. The proof of Proposition 4.1 does not rely on the anti-diffusive feature of the numerical scheme.

In Section 5 we shall present one-dimensional and two-dimensional numerical results of pure interface advection for fluids with complex or analytical EOSs that concur with Proposition 4.1.

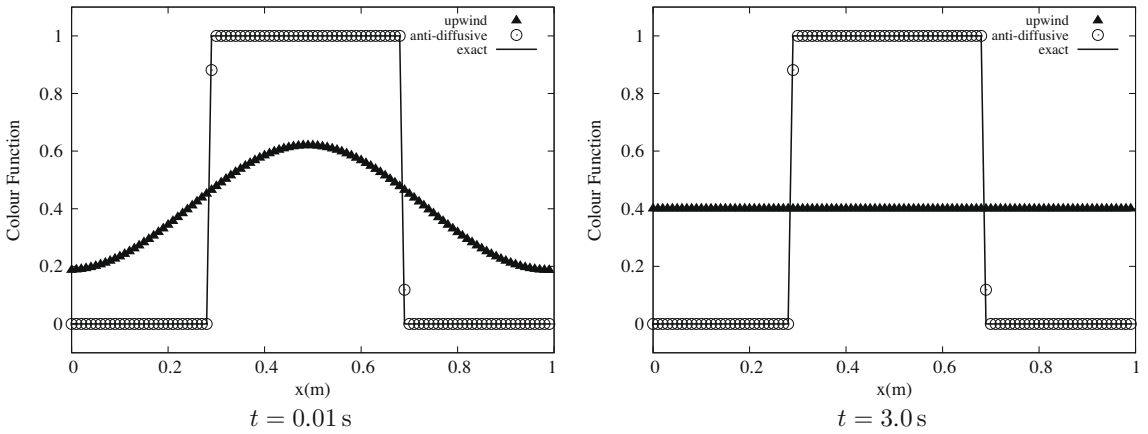

Fig. 3. One-dimensional advection test. Profiles of the color function obtained with the upwind scheme, the anti-diffusive scheme and the exact solution at instant $t \in \{0.01, 3.0\}$ s.

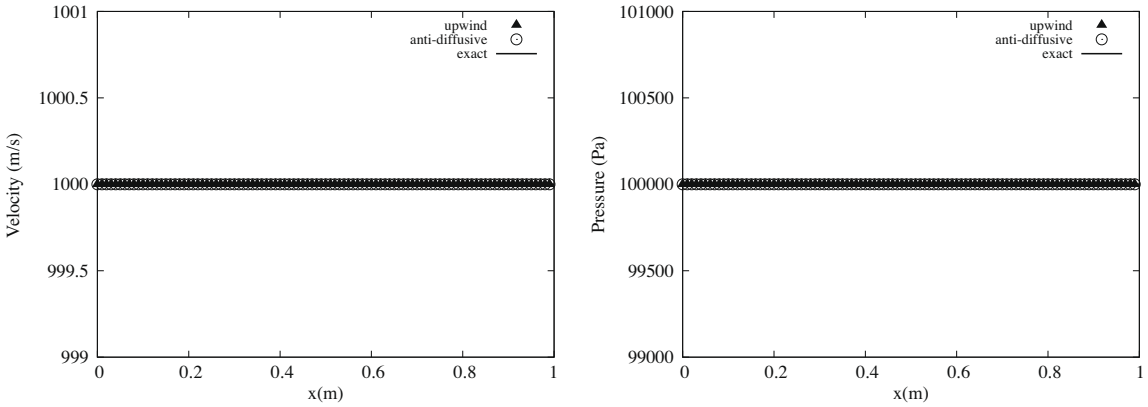

Fig. 4. One-dimensional advection test. Profiles of the velocity and the pressure obtained with the upwind scheme, the anti-diffusive scheme and the exact solution, at instant $t = 3.0$ s.

5. Numerical results

We present a selection of numerical tests performed with the anti-diffusive scheme and the classic upwind Lagrange–Remap solver for the five-equation model with isobaric closure. For both schemes, the two-dimensional tests have been achieved thanks to a simple directional splitting. In this case, we suppose that the domain is discretized over a Cartesian grid and we note $\mathbf{u} = (u_1, u_2)$ the velocity of the media. We set $\rho\mathbf{U} = [\rho, \rho u_1, \rho u_2, \rho e]^T, F_1(\rho\mathbf{U}, z) = [\rho u_1, \rho u_1^2 + P, \rho u_1 u_2, (\rho e + P)u_1]^T$ and $F_2(\rho\mathbf{U}, z) = [\rho u_2, \rho u_1 u_2, \rho u_2^2 + P, (\rho e + P)u_2]^T$. System (1) for two-dimensional problems is approximated by solving successively

$$\begin{cases} \partial_t \rho\mathbf{U} + \partial_{x_1} F_1(\rho\mathbf{U}, z) = 0, \\ \partial_t z + u_1 \partial_{x_1} z = 0, \end{cases} \quad \text{then} \begin{cases} \partial_t \rho\mathbf{U} + \partial_{x_2} F_2(\rho\mathbf{U}, z) = 0, \\ \partial_t z + u_2 \partial_{x_2} z = 0. \end{cases}$$

In the first step (resp. second step), the velocity component u_2 (resp. u_1) is passively advected and therefore the problem boils down to the one-dimensional case with an extra advected scalar. The overall stability and consistency properties are ensured by each directional step. The present method is limited to Cartesian meshes.

The following study is limited to the comparison of the anti-diffusive scheme against the upwind scheme for the following reasons: first, we believe that both schemes perform in a very similar way far from the interface. Numerical tests will help to shed some light on this matter. Second, there is a very broad range of numerical schemes and interface capture techniques, like Level Set techniques [47,30,31,9,46,45], Front Tracking [10,4,15,59], or VOF [14,18,29] methods, that would be worth comparing to the anti-diffusive scheme. Achieving such an exhaustive comparison would be very lengthy and is beyond the scope of the present work. Nevertheless we shall see in Section 5.7 that results obtained with the anti-diffusive scheme shows a strong agreement with both experimental results and previous works.

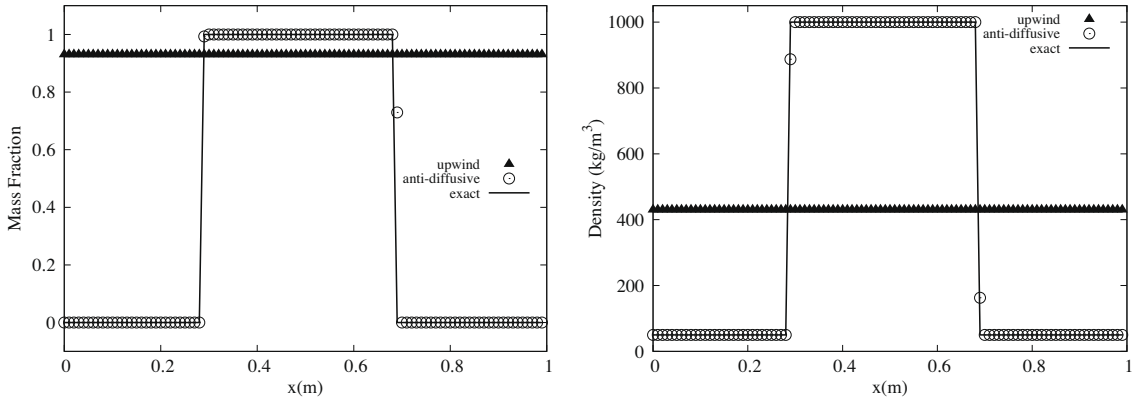

Fig. 5. One-dimensional advection test. Profiles of the mass fraction y and the density obtained with the upwind scheme, the anti-diffusive scheme and the exact solution, at instant $t = 3.0$ s.

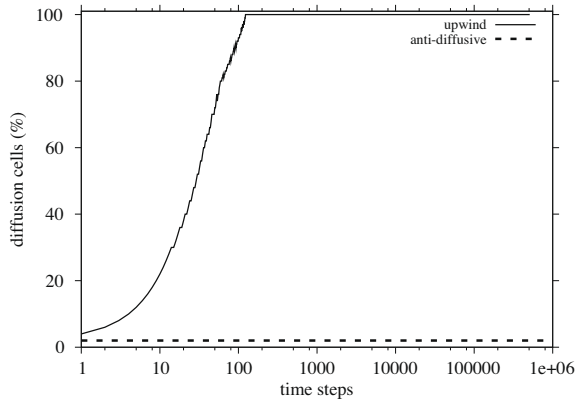

Fig. 6. One-dimensional advection test. Percent of cells in the domain where the color function z is numerically diffused versus the number of time steps (in log scale), for the upwind and the anti-diffusive scheme.

5.1. One-dimensional advection test

We consider a one-dimensional interface advection between two materials: the first fluid (denoted by fluid 0) is governed by a tabulated EOS and the second fluid (denoted by fluid 1) is a stiffened gas. For the sake of simplicity and ease of reproducibility we tabulated the following van der Waals gas:

$$P = \left(\frac{\gamma_0 - 1}{1 - b_0\rho}\right)(\rho\varepsilon + a_0\rho^2) - a_0\rho^2, \quad \gamma_0 = 1.4, \quad b_0 = 10^{-3}, \quad a_0 = 5.$$

The table data were obtained by discretizing the region of the (ρ, P)-plane delimited by $0 \leqslant \rho \leqslant 990$ and $10^4 \leqslant P \leqslant 10^9$ over a uniform grid of 1000×1000 nodes. The table gives the values of $\rho\varepsilon$ for each node (ρ, P) and the function $(\rho, P) \mapsto \rho\varepsilon$ is

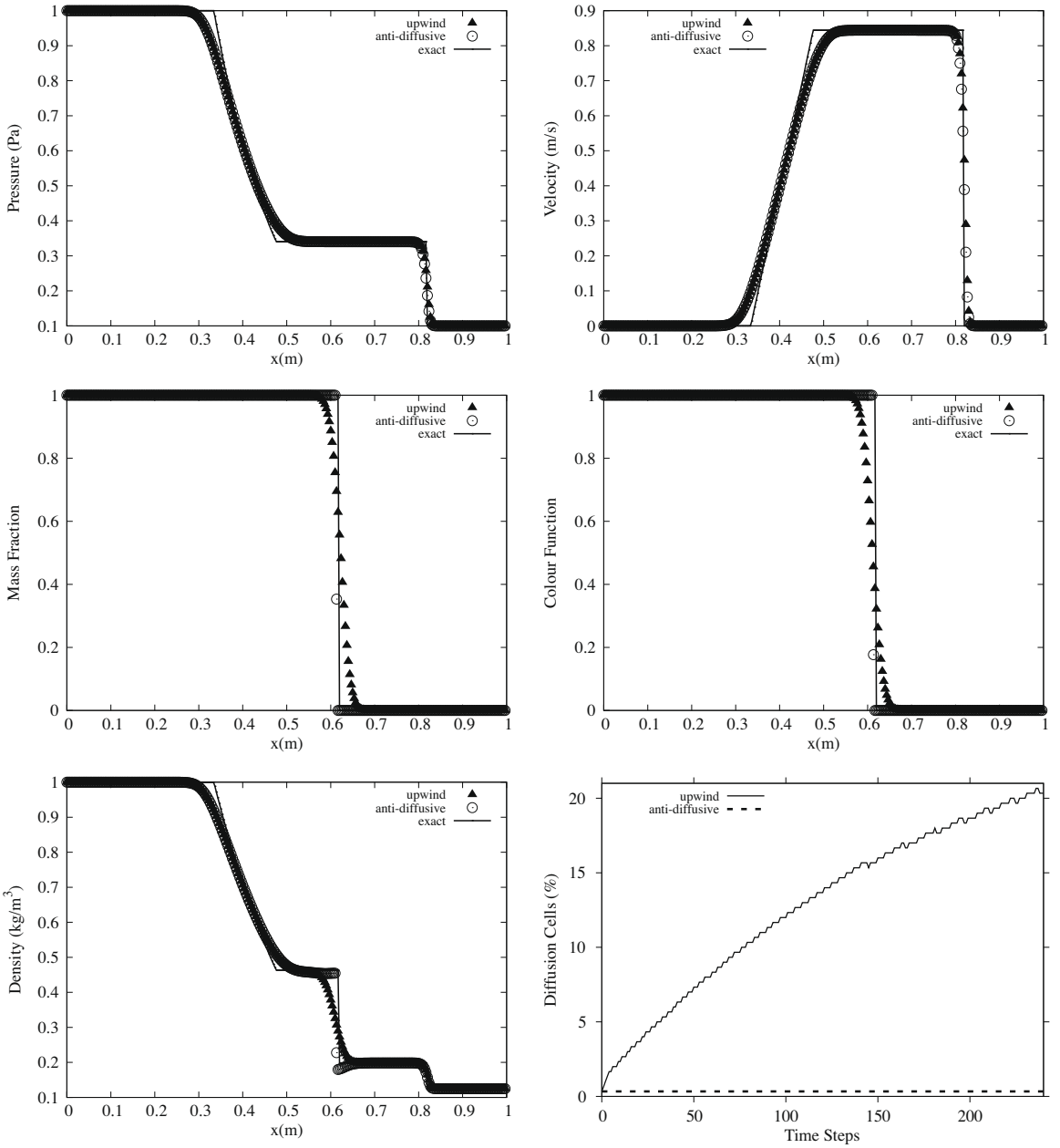

Fig. 7. Shock tube test with a 300-cell mesh. Profiles of the density, the pressure, the velocity, the mass fraction and the color function obtained with the upwind scheme, anti-diffusive scheme and the exact solution, at instant $t = 0.14$ s. Percent of cells in the domain where the color function z is numerically diffused versus the number of time steps for both upwind and anti-diffusive schemes.

provided thanks to a Q_1 interpolation. For the tabulated gas, the function $(\rho,\varepsilon)\mapsto P$ is defined implicitly and evaluated by means of a Newton method.

The fluid 1 is a stiffened gas whose EOS is given by the following analytical relation:

$$P = (\gamma_1 - 1)\rho\varepsilon - \gamma_1\pi_1, \quad \gamma_1 = 4.4, \quad \pi_1 = 6\times 10^8 \text{ Pa} \tag{41}$$

The pressure of the five-equation model with isobaric closure is then retrieved by solving the equation $P_0 = P_1$ with respect to the variable $\rho_1\varepsilon_1$ thanks to a dichotomy algorithm.

We consider a 1 m long one-dimensional domain with periodic boundary conditions. The initial condition depicts a one-dimensional fluid 1 bubble surrounded by fluid 0, namely

$$(\rho,u,P) = (50 \text{ kg m}^{-3}, 10^3 \text{ m s}^{-1}, 10^5 \text{ Pa}), \quad \text{for } x\in[0,0.3)\cup(0.7,1], \quad \text{at } t = 0 \text{ (fluid 0)},$$
$$(\rho,u,P) = (10^3 \text{ kg m}^{-3}, 10^3 \text{ m s}^{-1}, 10^5 \text{ Pa}), \quad \text{for } x\in[0.3,0.7], \quad \text{at } t = 0 \text{ (fluid 1)}.$$

The domain is discretized over a 100-cell mesh and we impose $C^{\text{CFL}} = 0.99$.

The color function profile obtained with the anti-diffusive solver remains very sharp throughout the computation (see Fig. 3). Indeed, at $t = 3.0$ s after 1524000 time steps, the initial pulse shape of the variable is preserved by the anti-diffusive scheme: only two cells are affected by numerical diffusion. Moreover, the position of the approximated pulse shows a very strong match with the exact solution.

Fig. 4 shows that the constant pressure and velocity profiles are preserved by the anti-diffusive scheme. This illustrates the ability of the solver to provide a good treatment of the iso-pressure and iso-velocity solutions, even in the case of complex and non-analytic EOSs.

One can notice in Fig. 5 that the density variable ρ and the mass fraction variable y both inherit the anti-diffusive property built for the variable z. Indeed, at $t = 3.0$ s, the pulse shape of both density and mass fraction is captured with no more than 2 cells of numerical diffusion.

The evolution of the numerical diffusion for the color function variable z throughout the computation is given in Fig. 6 thanks to the graph of the function $N\mapsto$ percent(N), where N is the number of time steps and percent(N) is the percent of cells where the variable z is numerically diffused. At an instant t^n, a cell i is counted as a cell with diffused value of z if

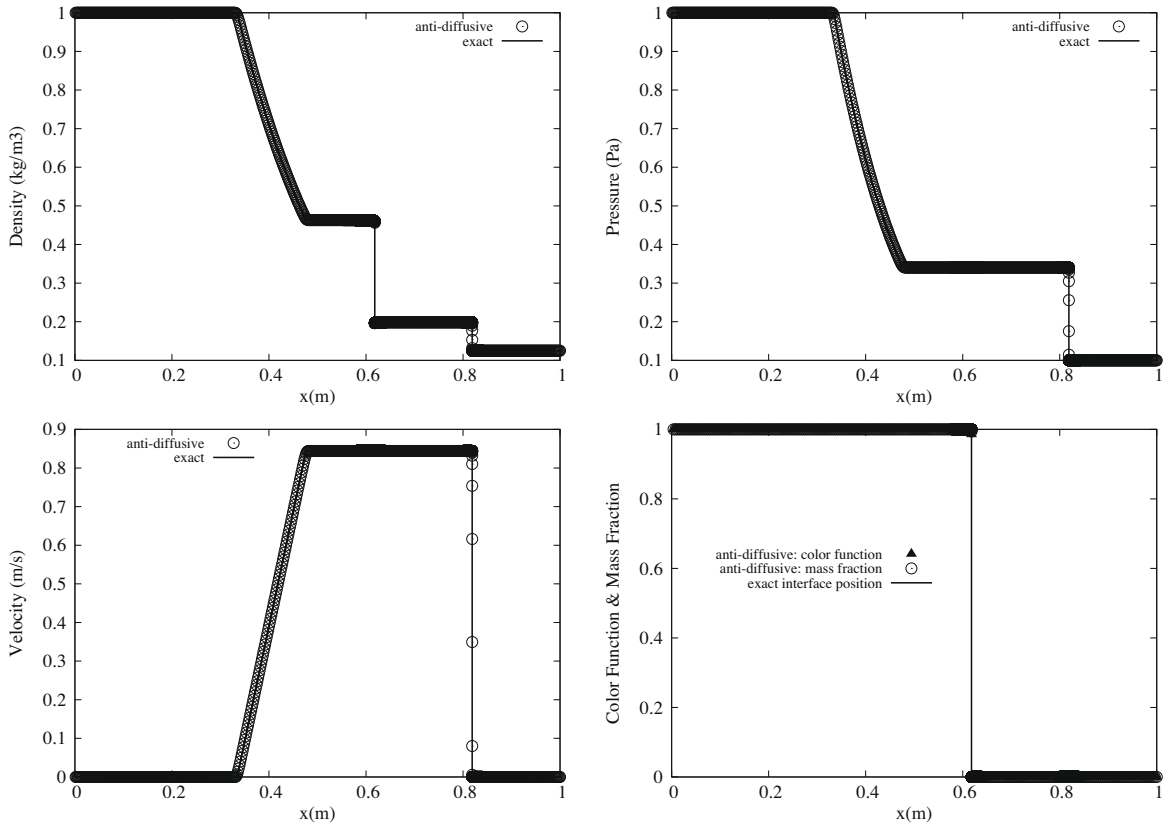

Fig. 8. Shock tube test with a 50000-cell mesh. Profiles of the density, the pressure, the velocity, the mass fraction and the color function for the shock tube test obtained with the anti-diffusive scheme and the exact solution, at instant $t = 0.14$ s.

$v < z_i^n < 1 - v, v = 10^{-6}$. This graph shows that the number of diffusion cells reaches the asymptotic value of 2% (2 diffusion cells) straight after the first time step with the anti-diffusive solver.

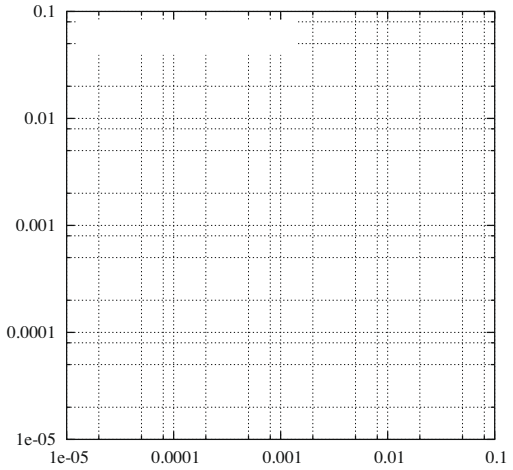

Table 1
Convergence rate estimates obtained with both upwind and anti-diffusive schemes, for the shock tube test of Section 5.2 at instant $t = 0.14$ s. The rates are computed thanks to a linear regression performed on the function $\ln(\Delta x) \mapsto \ln(E_{\Delta x}[q](t = 0.14)), q \in \{\rho, P, u, z, y\}$.

Variable	Convergence rate for the upwind scheme	Convergence rate for the anti-diffusive scheme
Pressure	0.819	0.830
Velocity	0.824	0.835
Density	0.656	0.833
Mass fraction y	0.478	1.042
Color function z	0.525	1.038

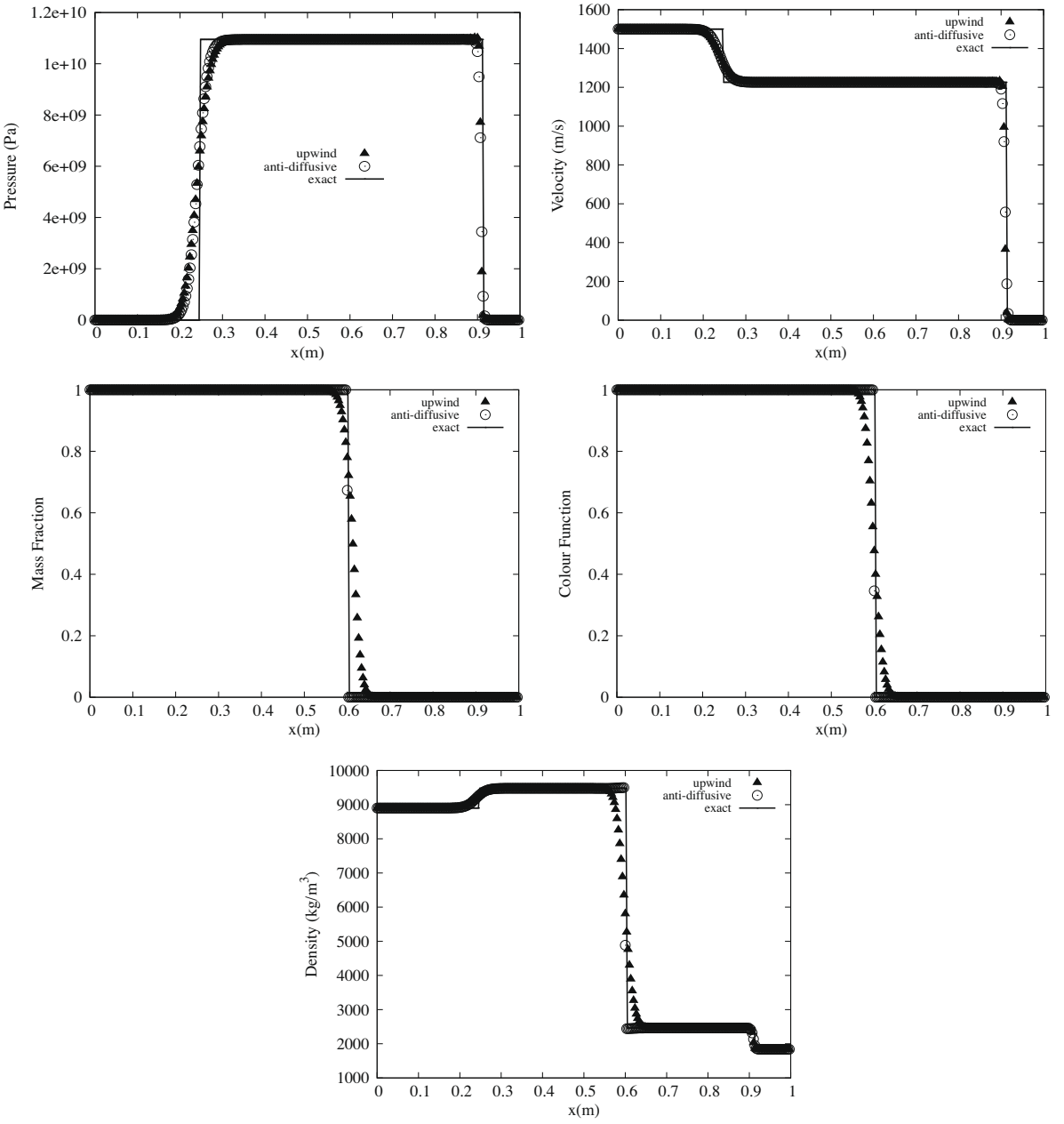

Fig. 10. One-dimensional impact problem. Profiles of the density, the pressure, the velocity, the mass fraction and the color function obtained with the upwind scheme, the anti-diffusive scheme and the exact solution, at $t = 85$ μs.

5.2. Shock tube test

We now test the anti-diffusive with a shock tube simulation that is derived from the classical test elaborated by Sod [53]. The test involves two perfect gases whose EOSs read

$$P_k = (\gamma_k - 1)\rho_k \varepsilon_k, \quad k = 0, 1. \tag{42}$$

At $t = 0$ both fluids are at rest in a 1 m long one-dimensional domain, separated by an interface located at $x = 0.5$ m. On each side of the interface, the initial fluid state is

$$(\gamma, \rho, u, P) = (1.4, 1.0\ \text{kg m}^{-3}, 0.0, 1.0\ \text{Pa}), \qquad \text{for } 0 \leqslant x < 0.5,$$
$$(\gamma, \rho, u, P) = (2.4, 0.125\ \text{kg m}^{-3}, 0.0, 0.1\ \text{Pa}), \quad \text{for } 0.5 \leqslant x \leqslant 1.$$

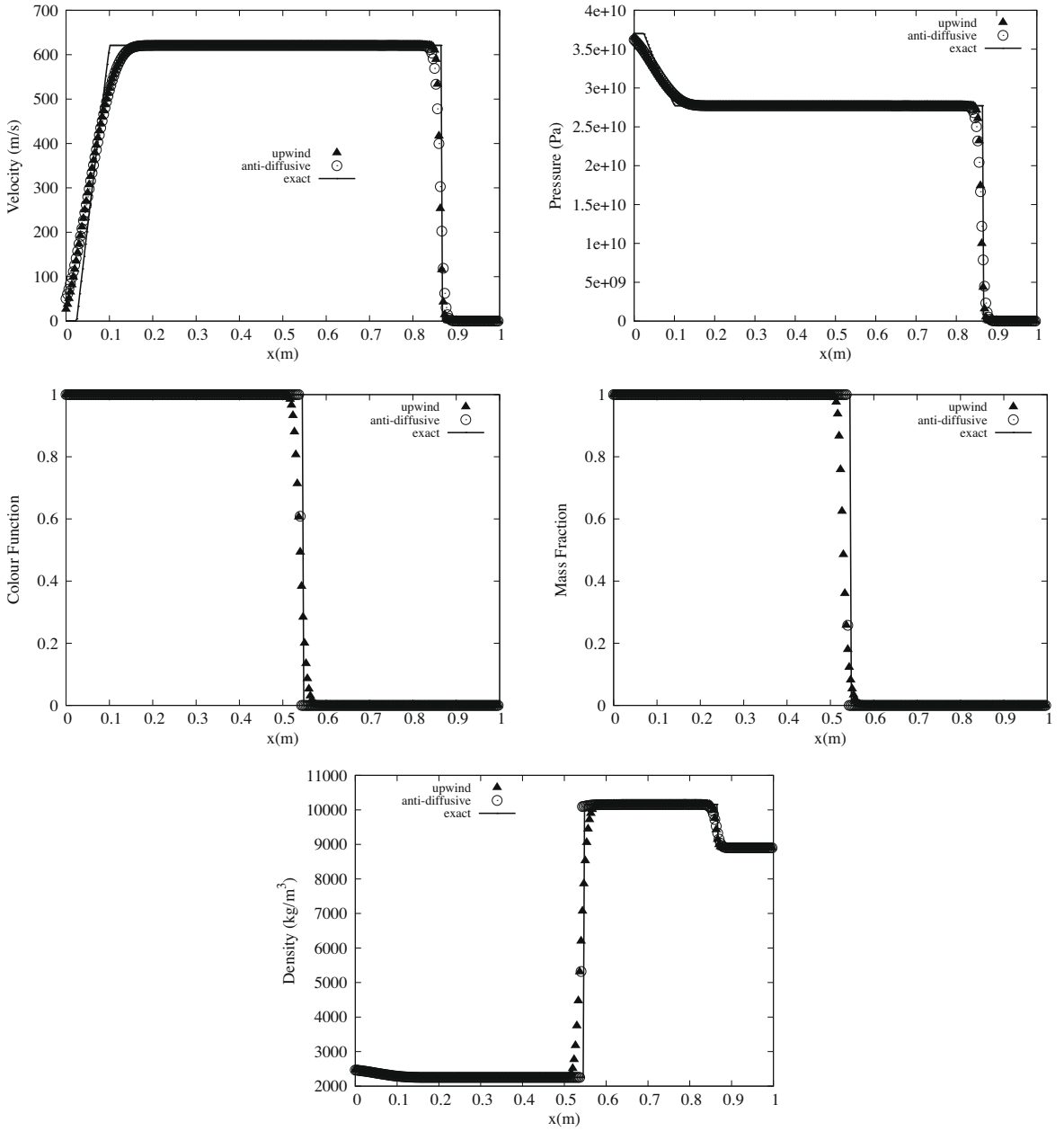

Fig. 11. Shock tube problem with the Cochran-Chan and the JWL gas. Profiles of the density, the pressure, the velocity, the mass fraction and the color function obtained with the upwind scheme, the anti-diffusive scheme and the exact solution, at $t = 73$ μs.

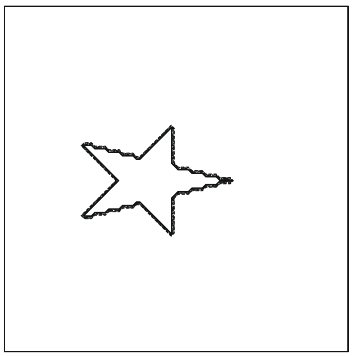

Fig. 12. Two-dimensional advection test. Profile of the color function at $t = 0$ s.

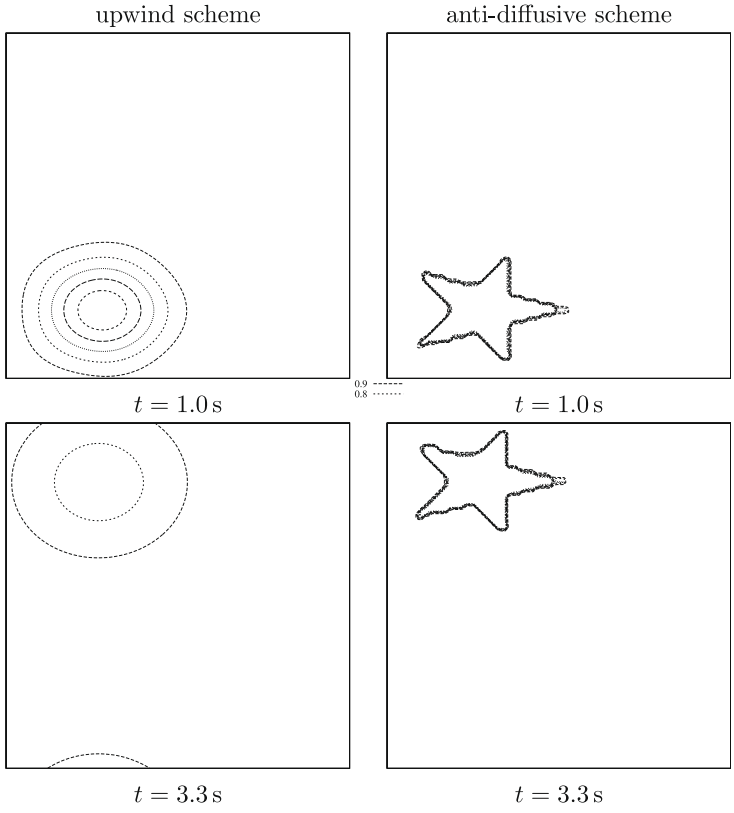

The domain is discretized over a 300-cell mesh and both boundary conditions are computed by maintaining constant states. Fig. 7 displays the results of the simulation at $t = 0.14$ s. For both pressure and density there is a good agreement between the anti-diffusive and the upwind solver. One can see that the interface is captured with at most two diffusion cells by the anti-diffusive solver for all the variables that experience a jump at the material interface, namely: the color function z, the mass fraction y and the density ρ. Far from the interface, the density profiles computed by both schemes coincide.

The above observations suggest that the anti-diffusive mechanism of the anti-diffusive scheme is only triggered at the contact discontinuity. For the shock and the rarefaction waves, the anti-diffusive scheme simply degenerates to the upwind scheme. This explains the similarities between both results. This statement is also consistent with the strong match between the pressure and the velocity computed by both schemes as these variables are not sensitive to the strength of the contact discontinuity. This phenomenon will be illustrated in the next tests.

We notice a slight undershoot at the contact discontinuity for the density. Fig. 8 displays the result obtained for the same test with a 50000-cell grid: as we refine the mesh, this flaw vanishes and all variables converge to the exact solution.

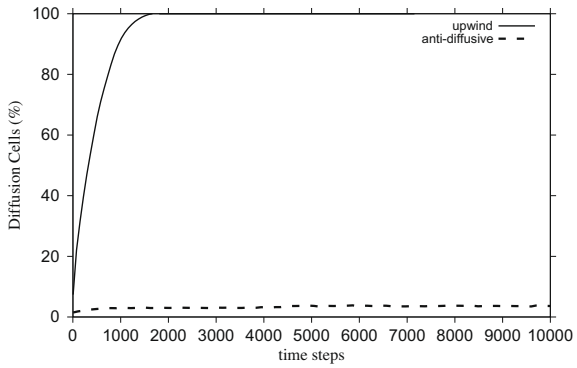

Fig. 14. Two-dimensional advection test. Percent of cells in the domain where the color function z is numerically diffused versus the number of time steps, for the upwind the and the anti-diffusive scheme.

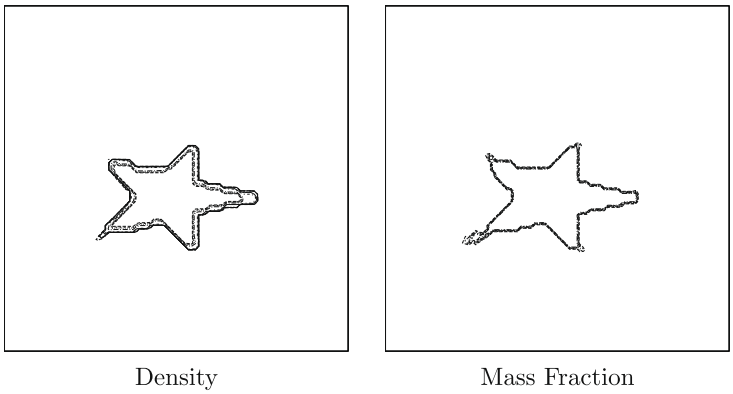

Fig. 15. Two-dimensional advection test. Iso-contours $\rho = \{0.05, 0.08, 0.5, 0.1, 1.0, 5.0, 7.0, 8.0, 9.0\}$ for the density ρ and isocontours $y = \{0.1, 0.2, 0.3, 0.4, 0.5, 0.6, 0.7, 0.8\}$ for the mass fraction y obtained with the anti-diffusive scheme at instant $t = 7.0$ s.

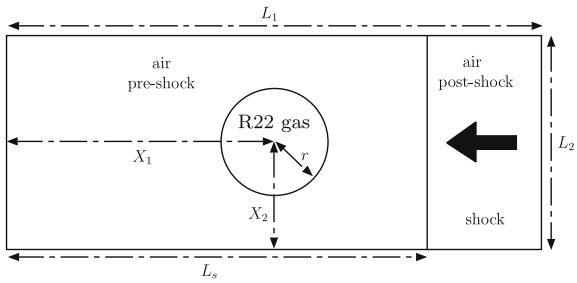

Fig. 16. Air-R22 shock/cylinder interaction test. Description of the initial conditions.

The evolution of the numerical diffusion is displayed in Fig. 7 and is quite coherent with the results of Section 5.1. After the very first time steps, the shock departs from the interface, which becomes driven by the advection at the local velocity. Then, the percentage of diffusion cells reaches instantaneously an asymptotic value of 0.33%, i.e. one diffusion cell.

5.3. Convergence test

The shock tube test of Section 5.2 is now used to investigate the convergence rate of the anti-diffusive scheme. We obtain a converge rate estimate of the scheme by computing the relative error of the approximate solution in $L^1(0,1)$ norm for different space steps. Let q be a computed variable, we note q^{exact} the exact solution and $q_{\Delta x}$ the approximate solution computed on a Δx space step mesh. The $L^1(0,1)$ relative error $E_{\Delta x}[q]$ for the variable q and the space step Δx is defined by $t \mapsto E_{\Delta x}[q](t) = \|q^{\text{exact}}(\cdot,t) - q_{\Delta x}(\cdot,t)\|_{L^1(0,1)} / \|q^{\text{exact}}(\cdot,t)\|_{L^1(0,1)}$. Fig. 9 displays the relative error in log scale of the variables ρ, u, P, y and z at instant $t = 0.14\,s$ for the range of space steps $\Delta x^{-1} \in \{300, 500, 10^3, 5\times10^3, 8.5\times10^3, 10^4, 15\times10^3,$

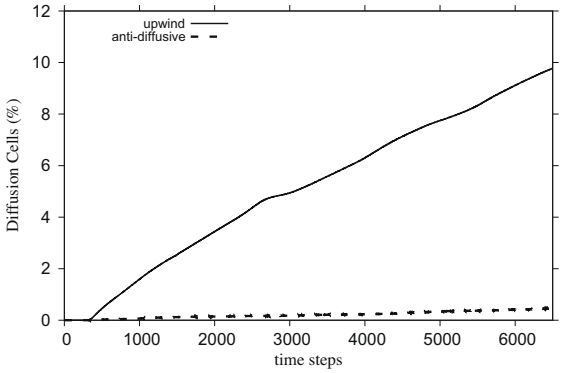

Fig. 17. Air-R22 cylinder/bubble interaction test. Percent of cells in the domain where the color function z is numerically diffused versus the number of time steps for both upwind and anti-diffusive scheme.

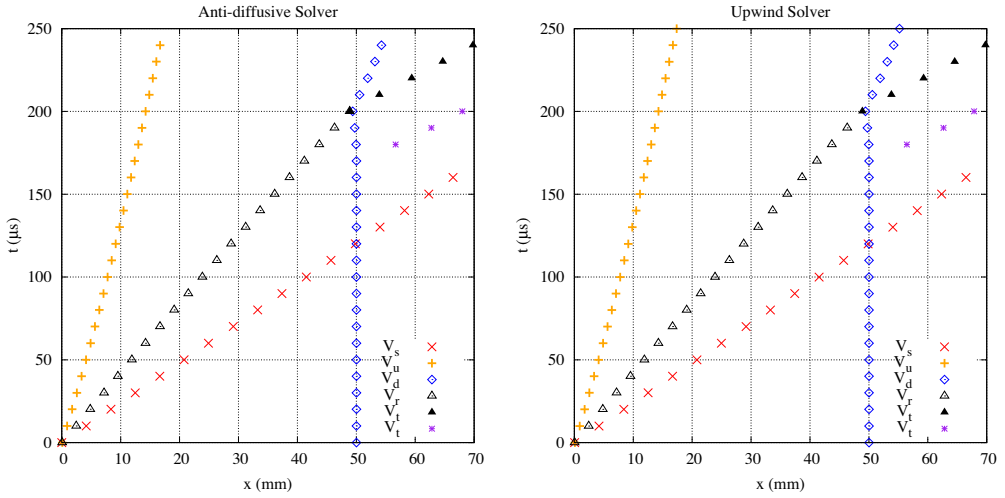

Fig. 18. Evolution in the space-time plan of the following wave fronts: the incident shock wave (marked with a "×" symbol), the upstream interface position (marked with a "+" symbol), the downstream interface position (marked with a "◇" symbol), the refracted shock wave (marked with a "△" symbol) and the transmitted shock waves (marked with a "▲" and a "*" symbol). The space measures refer to the distance between the wave front location and the first contact position between the cylinder and the incident shock wave.

Table 2
Air-R22 shock/cylinder interaction test. EOSs coefficients and initial data.

Location	Density (kg m^{-3})	Pressure (Pa)	u_1 (m s^{-1})	u_2 (m s^{-1})	γ
Air (post-shock)	1.686	1.59×10^5	−113.5	0	1.4
Air (pre-shock)	1.225	1.01325×10^5	0	0	1.4
R22	3.863	1.01325×10^5	0	0	1.249

$20 \times 10^3, 30 \times 10^3, 50 \times 10^3\}$. We computed the value of the convergence rates by performing a simple linear regression. Results are gathered in Table 1. For the pressure and velocity variables that are "blind" to the contact discontinuity wave strength the convergence rates are quite similar with both schemes. However, the error for the variables y and z is reduced by more than one decade for small values of Δx and we obtain convergence rates which are close to 1.0. This convergence improvement is visible with the density variable that is sensitive to every waves of the system for small values of Δx.

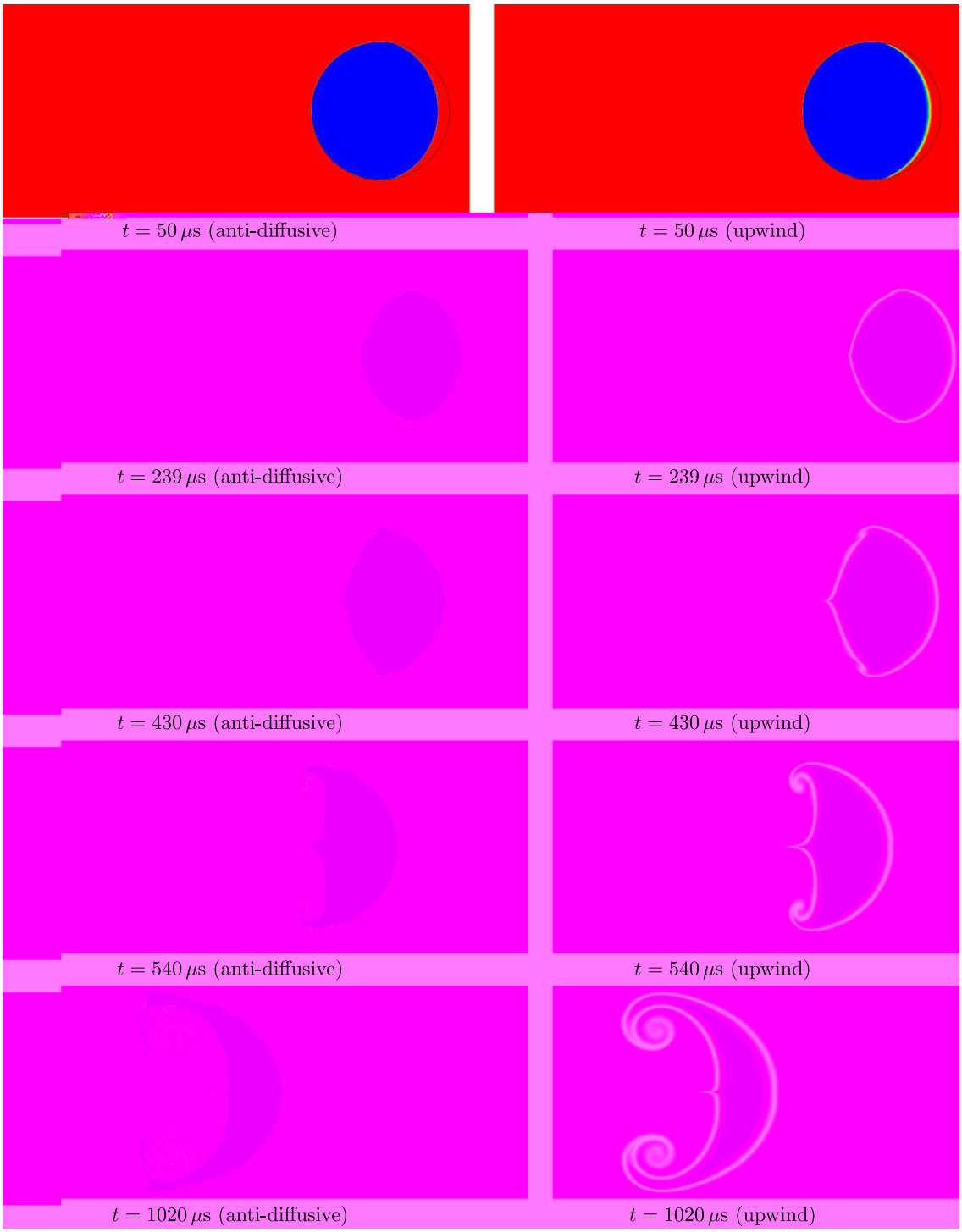

Fig. 19. Air-R22 shock/cylinder interaction test. Mapping of the color function z for both upwind and anti-diffusive solvers. The initial position of the cylinder is represented by a solid black line. The instant $t = 0$ is chosen to coincide with the time when the shock hits the cylinder.

5.4. One-dimensional impact problem between two Mie-Grüneisen materials

We consider a Riemann problem examined by Refs. [27,34,3] that aims at simulating the impact of a copper plate onto an inert solid. We suppose that both components are governed by a Mie-Grüneisen-type EOS:

$$P(\rho,\varepsilon) = \Gamma(\rho)\rho(\varepsilon - \varepsilon^{\text{ref}}(\rho)) + P^{\text{ref}}(\rho). \tag{43}$$

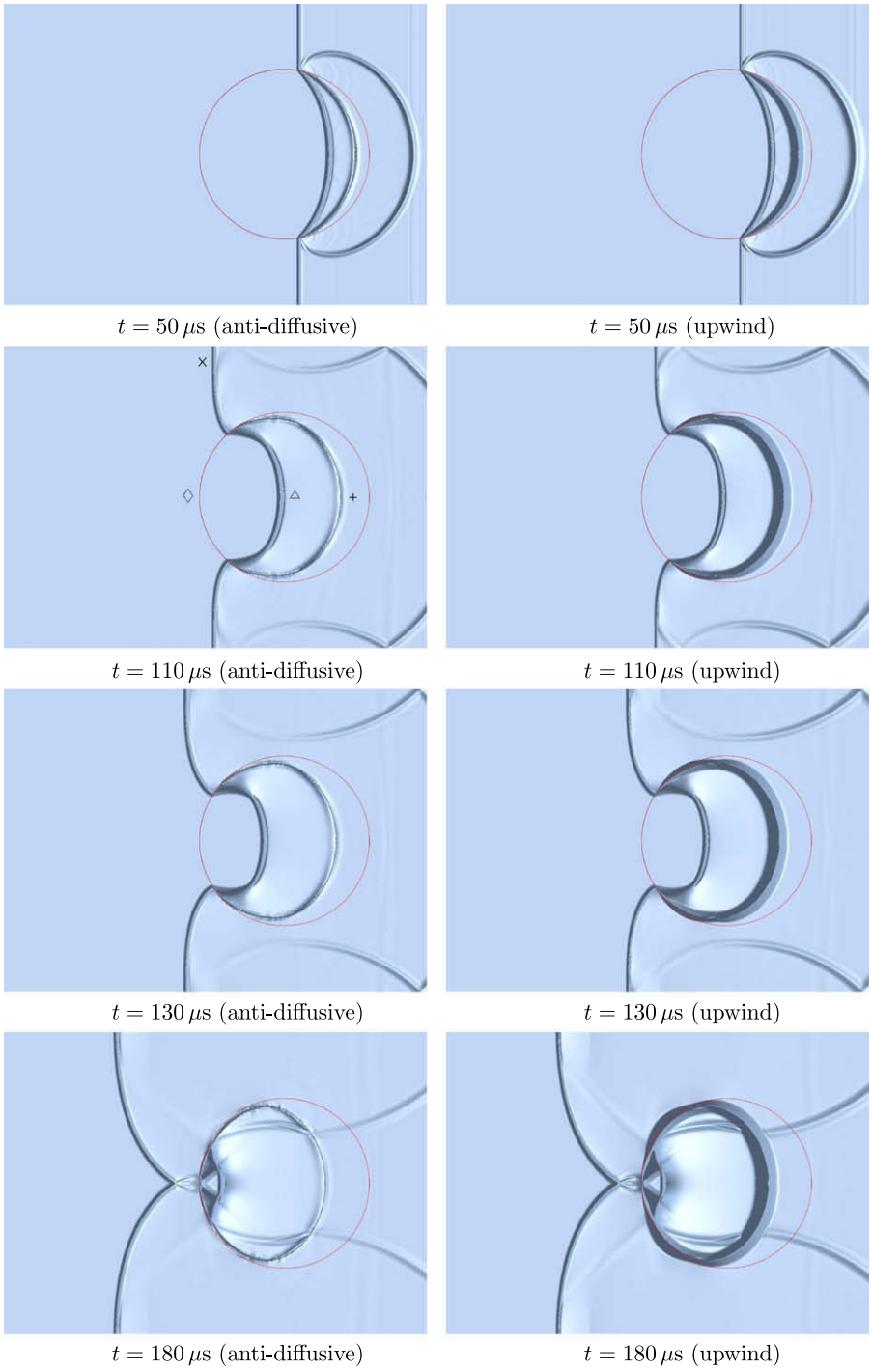

Fig. 20. Air-R22 shock/cylinder interaction test. Schlieren diagram for both upwind and anti-diffusive solvers. The initial position of the cylinder is represented by a solid red line. The instant $t = 0$ is chosen to coincide with the time when the shock hits the cylinder. (For interpretation of the references to color in this figure legend, the reader is referred to the web version of this article.)

Each material is supposed to verify the Cochran-Chan law, which provides the following form for the functions $\Gamma, \varepsilon^{\text{ref}}$ and P^{ref}:

$$\varepsilon^{\text{ref}}(\rho) = \sum_{r=1,2} \frac{(-1)^r \mathscr{A}_r}{(1-\mathscr{E}_r)\rho^{\text{ref}}} \left[\left(\frac{\rho^{\text{ref}}}{\rho} \right)^{1-\mathscr{E}_r} - 1 \right] - e^{\text{ref}}, \quad P^{\text{ref}}(\rho) = \sum_{r=1,2} (-1)^{k+1} \mathscr{A}_r \left(\frac{\rho^{\text{ref}}}{\rho} \right)^{-\mathscr{E}_r}, \quad \Gamma(\rho) = \Gamma^{\text{ref}}.$$

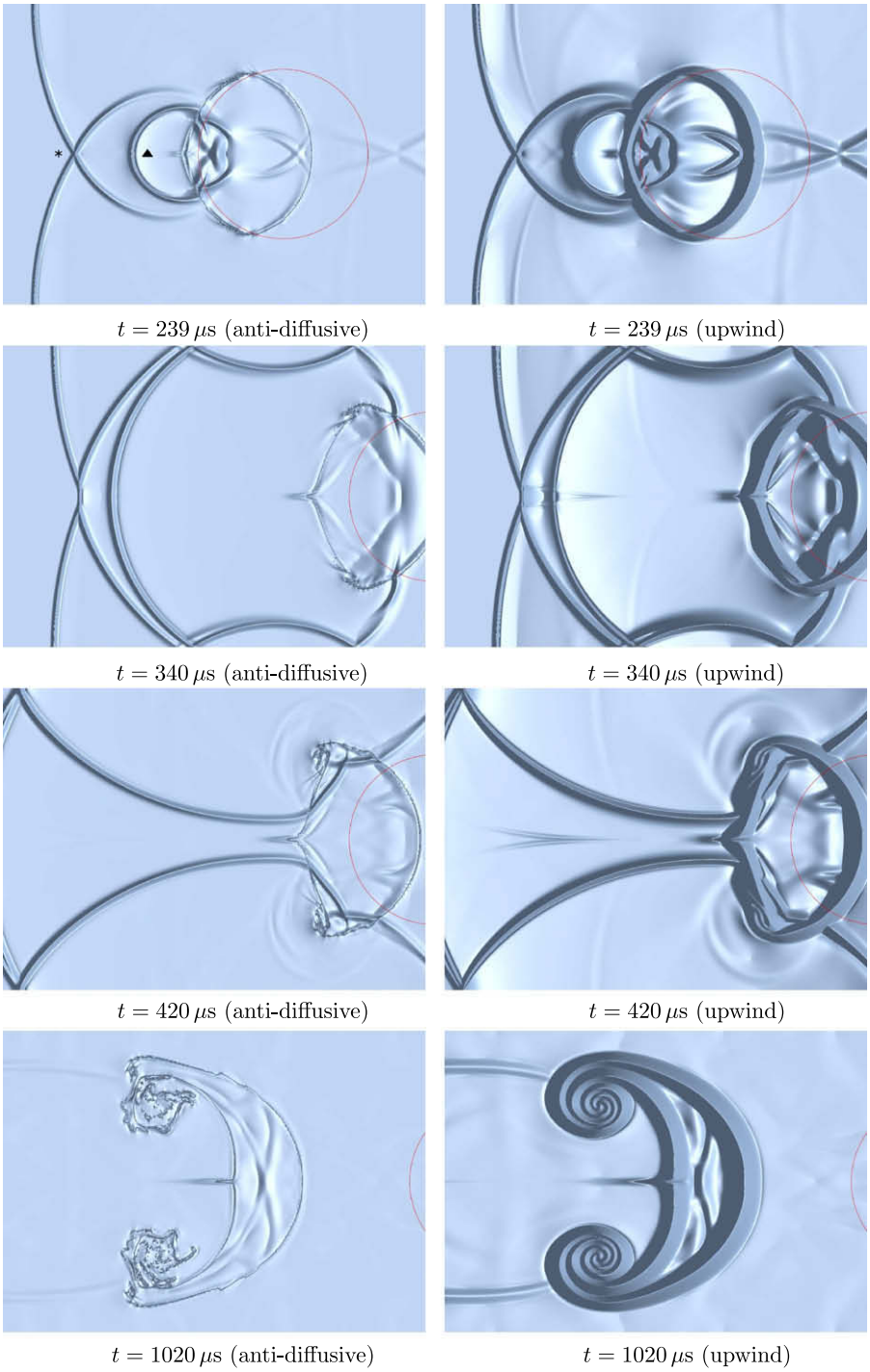

Fig. 21. Air-R22 shock/cylinder interaction test. Schlieren diagram for both upwind and anti-diffusive solvers. The initial position of the cylinder is represented by a solid red line. The instant $t = 0$ is chosen to coincide with the time when the shock hits the cylinder. (For interpretation of the references to color in this figure legend, the reader is referred to the web version of this article.)

In our case, we have

$$(\Gamma^{\text{ref}}, \rho^{\text{ref}}, e^{\text{ref}}, \mathscr{A}_1, \mathscr{A}_2, \mathscr{E}_1, \mathscr{E}_2)_{\text{copper}} = (2.0, 8900.0, 117900.0, 1.45667 \times 10^{11}, 1.47751 \times 10^{11}, 2.994, 1.994),$$
$$(\Gamma^{\text{ref}}, \rho^{\text{ref}}, e^{\text{ref}}, \mathscr{A}_1, \mathscr{A}_2, \mathscr{E}_1, \mathscr{E}_2)_{\text{solid}} = (0.93, 1840.0, 326100.0, 1.2871 \times 10^{10}, 1.34253 \times 10^{10}, 4.1, 3.1).$$

The solution of this problem is composed by a leftward-travelling shock wave, a contact discontinuity and a rightward-travelling shock wave. The computational domain is a 1 m long domain. At $t = 0$ the copper lies in the region $0 \leqslant x \leqslant 0.5$ with a velocity $u = 1500$ m. s^{-1} and a density $\rho = 8900$ kg m^{-3}, while the inert solid is at rest in the region $0.5 < x \leqslant 1$, with a density $\rho = 1840$ kg m^{-3}. The pressure is initially $P = 10^5$ Pa in the whole domain.

Fig. 10 displays the simulation results obtained at $t = 85$ μs with a 300-cell grid. Far from the interface the approximate solution obtained with both anti-diffusive scheme and upwind scheme are quite similar. The anti-diffusive solver succeeds

Table 3
Comparison of the computed wave velocities obtained thanks to both upwind and anti-diffusive with the numerical results presented in [25,35] and the experimental results of [13]. The velocities of the incident shock wave, the refracted shock wave, the transmitted shock wave, the initial upstream position, the final upstream position, the initial downstream position and the final downstream position are denoted, respectively, by $V_s, V_R, V_T, V_{ui}, V_{uf}, V_{di}, V_{df}$.

Velocity (m/s)	V_s	V_R	V_T	V_{ui}	V_{uf}	V_{di}	V_{df}
Experiment [13]	415	240	540	73	90	78	78
Quirk and Karni [25]	420	254	560	74	90	116	82
Shyue [35] (tracking)	411	243	538	64	87	82	60
Shyue [35] (capturing)	411	244	534	65	86	98	76
Upwind solver	411	243	524	66	86	83	62
Anti-diffusive solver	411	243	525	65	86	85	64

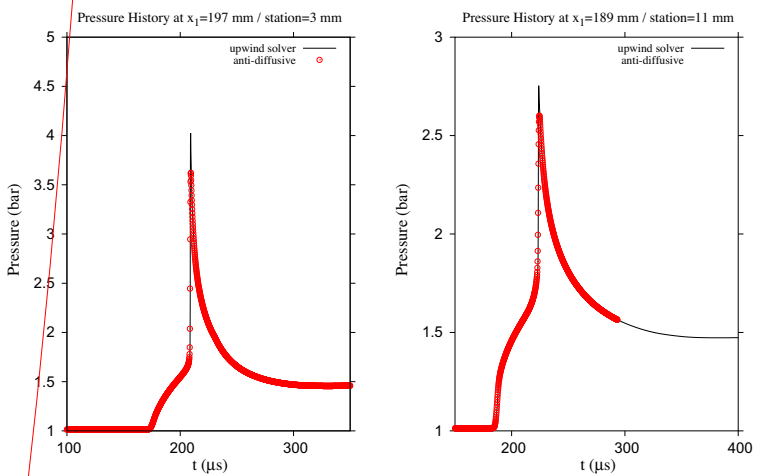

in controlling the numerical diffusion of the interface with a single diffusion cell while the upwind scheme captures the interface in a 56-cell region. The variables ρ and y which are sensitive to the contact discontinuity also approximate the interface with a single cell. Moreover, no spurious oscillations appear at the interface for the pressure or the velocity.

5.5. Shock tube problem with two Mie-Grüneisen materials

We now turn to another Riemann problem involving two Mie-Grüneisen components. This test has been presented in [27,34] and it involves the same Cochran-Chan material modelling copper that was used in Section 5.4 with a Jones–Wilkins–Lee (JWL) material modelling a gaseous explosive. The EOS for the JWL gas reads

$$\Gamma(\rho) = \Gamma^{\text{ref}}, \quad \varepsilon^{\text{ref}}(\rho) = \sum_{r=1,2} \frac{\mathscr{A}_r}{\mathscr{R}_r \rho^{\text{ref}}} \exp\left[-\mathscr{R}_r \frac{\rho^{\text{ref}}}{\rho}\right] - e^{\text{ref}}, \quad P^{\text{ref}}(\rho) = \sum_{r=1,2} \mathscr{A}_r \exp\left[-\mathscr{R}_r \frac{\rho^{\text{ref}}}{\rho}\right],$$

where we have

$$\Gamma^{\text{ref}} = 0.25, \quad \mathscr{A}_1 = 854.5 \times 10^9, \quad \mathscr{A}_2 = 20.5 \times 10^9, \quad \mathscr{R}_1 = 4.6, \quad \mathscr{R}_2 = 1.35, \quad \rho^{\text{ref}} = 1840, \quad e^{\text{ref}} = 8149.158 \times 10^3.$$

The domain is 1 m long and at $t = 0$, the interface is located at $x = 0.5$ m. The explosive is initially on the left side of the interface while the copper is on the right side. The state variables are set as follows:

$$(\rho, u, P) = (2485.37 \text{ kg m}^{-3}, 0.0, 3.7 \times 10^{10} \text{ Pa}), \quad \text{for } 0 \leqslant x \leqslant 0.5 \text{ at } t = 0,$$
$$(\rho, u, P) = (8900 \text{ kg m}^{-3}, 0.0, 10^5 \text{ Pa}), \quad \text{for } 0.5 < x \leqslant 1 \text{ at } t = 0.$$

The computational domain is discretized with 300 cells and the results obtained at $t = 73$ μs are displayed in Fig. 11. The solution is composed of a leftward-going rarefaction, a contact discontinuity and a rightward-going shock wave. The results of the upwind scheme and the anti-diffusive scheme coincide for the rarefaction and the shock. In both case, no oscillations occur at the interface. The interface is discretized with a single diffusion cell at $t = 73$ μs, while it is spread over 37 cells with the upwind scheme. The anti-diffusion mechanism also works for the variables y and ρ as in the previous tests.

5.6. Two-dimensional advection test

The present simulation aims at testing the ability of the anti-diffusive scheme to deal with pure interface advection in a two-dimensional case. We consider a 1 m × 1 m square domain that contains two perfect gases whose EOS verify relation (42). Initially both gases are separated by a star shaped interface (see Fig. 12) as follows: let us define

$$\mathscr{A} = \mathscr{A}_1 \cup \mathscr{A}_2, \quad \text{with} \begin{cases} \mathscr{A}_1 = \left\{(x_1, x_2) \in [0,1]^2 \text{ such that } \frac{1}{3} - \left|x_1 - \frac{1}{2}\right| < x_2 < \frac{2}{3} - 4\left|x_1 - \frac{1}{2}\right|\right\}, \\ \mathscr{A}_2 = \left\{(x_1, x_2) \in [0,1]^2 \text{ such that } \frac{1}{3} - \left|x_1 - \frac{1}{2}\right| < x_2 < \frac{1}{2}\right\} \end{cases}$$

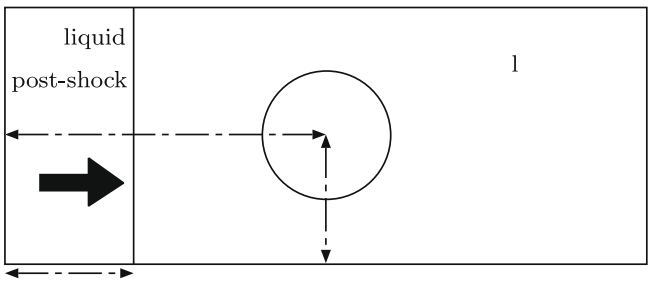

Table 4
Liquid–gas shock/bubble interaction test. EOS coefficients and initial data.

Location	Density (kg m^{-3})	Pressure (Pa)	u_1 (m s^{-1})	u_2 (m s^{-1})	γ	π (Pa)
Liquid (post-shock)	1030.9	3×10^9	300.0	0.0	4.4	6.8×10^8
Liquid (pre-shock)	1000.0	10^5	0.0	0.0	4.4	6.8×10^8
Air	1.0	10^5	0.0	0.0	1.4	0.0

at $t = 0$ we set

$$(\gamma, \rho, u_1, u_2, P) = \left(4.4, 10.0\ \text{kg m}^{-3}, \sqrt{2}/2\ \text{m s}^{-1}, \sqrt{3}/2\ \text{m s}^{-1}, 1\ \text{Pa}\right), \quad \text{for } x \in \mathscr{A},$$
$$(\gamma, \rho, u_1, u_2, P) = \left(1.4, 0.01\ \text{kg m}^{-3}, \sqrt{2}/2\ \text{m s}^{-1}, \sqrt{3}/2\ \text{m s}^{-1}, 1\ \text{Pa}\right), \quad \text{for } x \notin \mathscr{A}.$$

The computations are performed on a 100×100 mesh with periodic boundary conditions. The mesh was purposely chosen so as to check how the scheme manages sharp interfaces on a coarse grid.

The uniform pressure and velocity fields induce a translation motion of the interface across the domain. Fig. 13 shows isocontours of the color function z obtained with both solvers. The anti-diffusive scheme succeeds quite well in preserving both the sharpness and the overall shape of the interface despite the low resolution of the grid. The evolution of the number of diffusion cells is displayed in Fig. 14. After 10000 time steps, the percentage of diffused cells is only 3.75% for the anti-diffusive scheme.

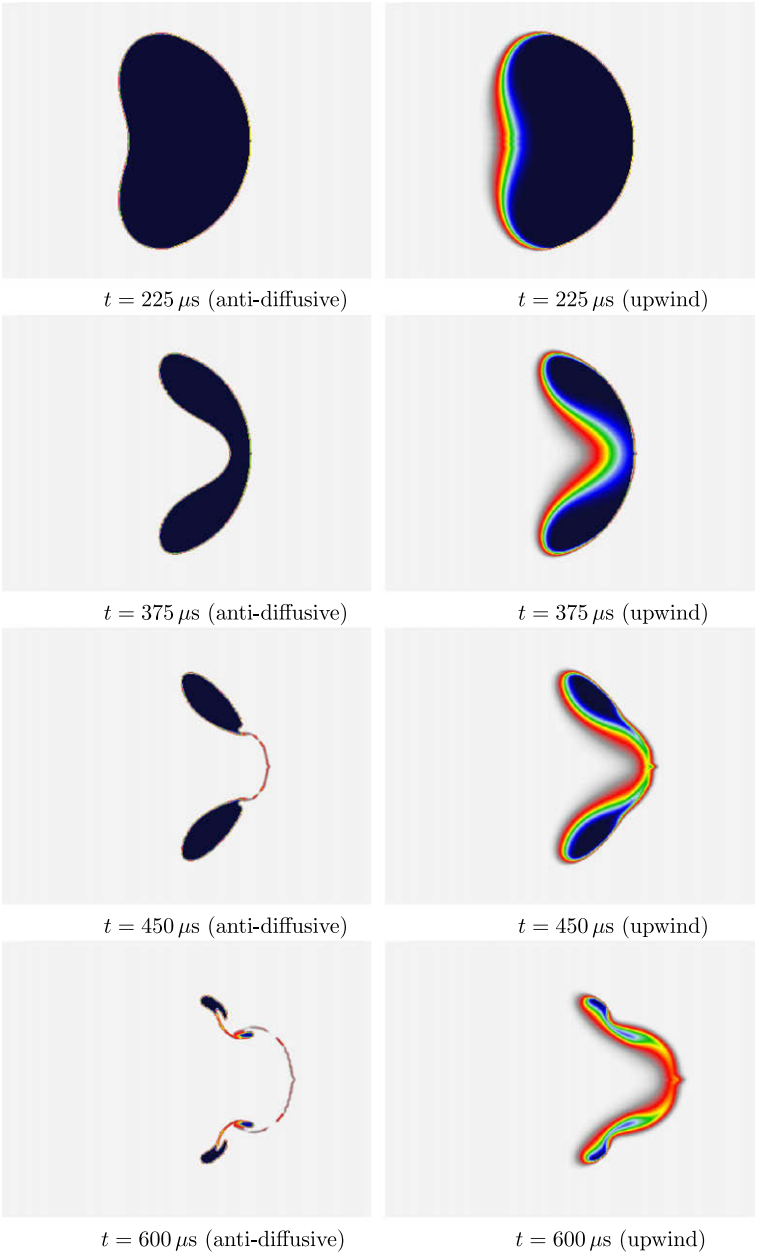

Fig. 24. Liquid–gas shock/bubble interaction test. Mapping of the color function z for both upwind and anti-diffusive solvers.

The velocity a
$t = 7.0$ s, the rela
the anti-diffusive
profile is altered l

ed by the anti-diffusive scheme as in the previous one-dimensional tests: at
6×10^{-9} for the pressure and 1.5×10^{-9} for the velocity. We observe that
s for both density ρ and mass fraction y as shown in Fig. 15 although their
h.

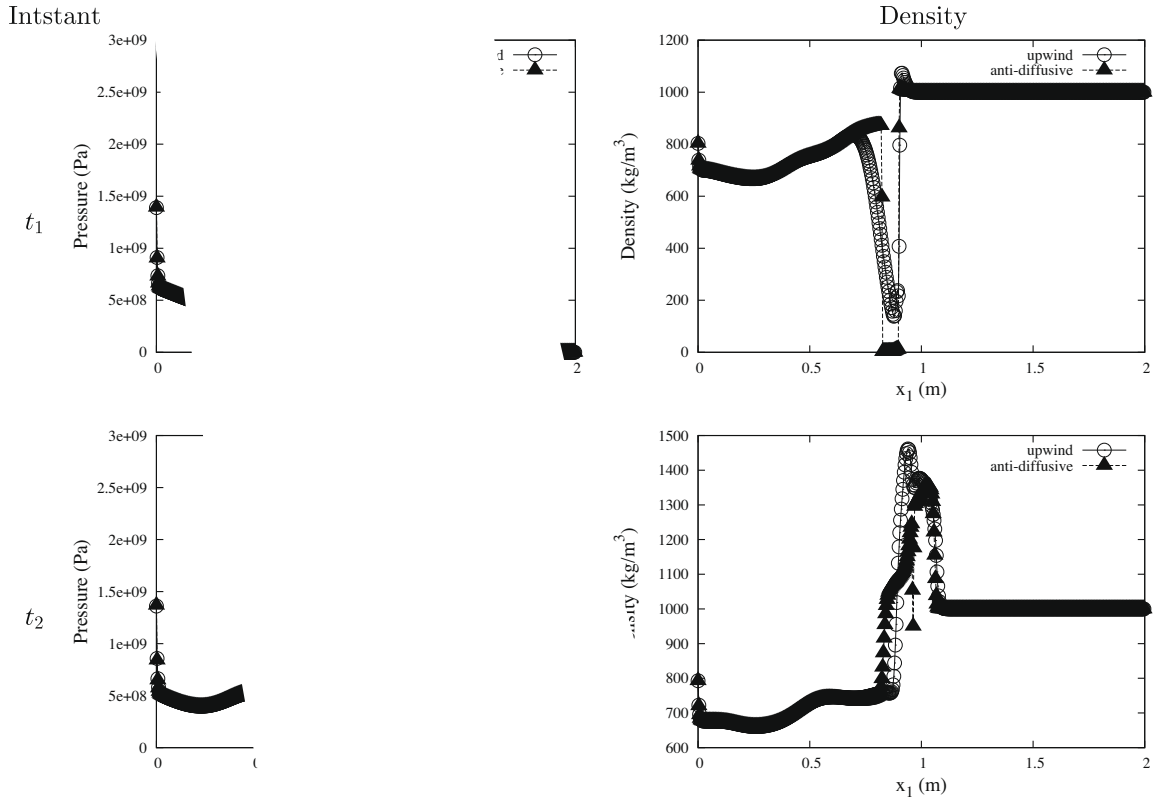

Fig. 25. Liquid–gas shock/bubble inter
at instants $(t_1, t_2) = (375, 450)$ µs.

ɪ the $x_2 = 0.5$ m axis with both upwind and anti-

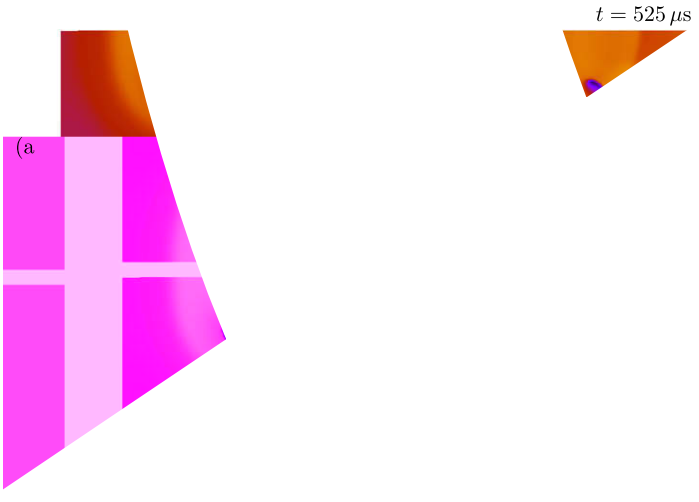

5.7. Air-R22 shock/cylinder interaction test

We now present a two-dimensional test that consists in simulating the impact of a Mach 1.22 shock travelling through air onto a cylinder of R22 gas. This test aims at simulating the experiment of [13] and has been considered by several authors such as [25,35]. Similar simulations are available in [1,28,9,33,3,37,49,12]. The initial conditions are depicted in Fig. 16: a cylinder of R22 is surrounded by air within a $L_1 \times L_2$ rectangular domain. At $t = 0$, the cylinder is at rest and with its center located at (X_1, X_2). We denote by r the initial radius of the cylinder. The planar shock is initially located at $x_1 = L_s$ and moves from right to left towards the cylinder. The parameters for this test are

$$L_1 = 445 \text{ mm}, \quad L_2 = 89 \text{ mm}, \quad L_s = 275 \text{ mm}, \quad X_1 = 225 \text{ mm}, \quad X_2 = 44.5 \text{ mm}, \quad r = 25 \text{ mm}.$$

Both R22 and air are modelled by two perfect gases whose coefficients γ and initial states are given in Table 2. The domain is discretized with a 5000×1000 regular mesh. Top and bottom boundary conditions are set to solid walls while we use constant state boundary conditions for the left and right boundaries.

The shock reaches the R22 bulk after approximately 60 μs, in the following we shall consider this instant as the instant $t = 0$. Fig. 19 displays the evolution cylinder shape obtained with both the anti-diffusive and the upwind solver. The profiles are obtained thanks to a mapping of the color function values and do not involve any interface reconstruction post-treatment or iso-contours computation. The overall location of the bulk is quite similar for both schemes. The shape of the vortex pair is numerically diffused into regular rounded shapes for the upwind scheme. The anti-diffusive solver succeeds in confining the interface within a very thin layer of cells and provides a different vortex pair shape with fine irregular structures that agrees with the simulations of [35] and the experimental results [13]. The percent of cells containing a numerically diffused value of z is displayed in Fig. 17: after 6800 time steps, the diffusion percent is 10% with the upwind scheme, while it is only 0.5% with the anti-diffusive solver. The continuous growth of the interface diffusion with the anti-diffusive scheme can be explained by the stretching of the interface during the motion. The perimeter of the bulk increases, this implies that the number of surrounding diffusion cells increases as well.

Table 5
Underwater explosion test. Initial conditions and EOSs parameters.

Fluid	Density (kg m^{-3})	Pressure (Pa)	γ	π (Pa)
Air above the water surface	1.225	1.011325×10^5	1.4	0.0
Gas inside the bubble	1250.0	10^9	1.4	0.0
Water	1000.0	1.011325×10^5	4.4	6.8×10^8

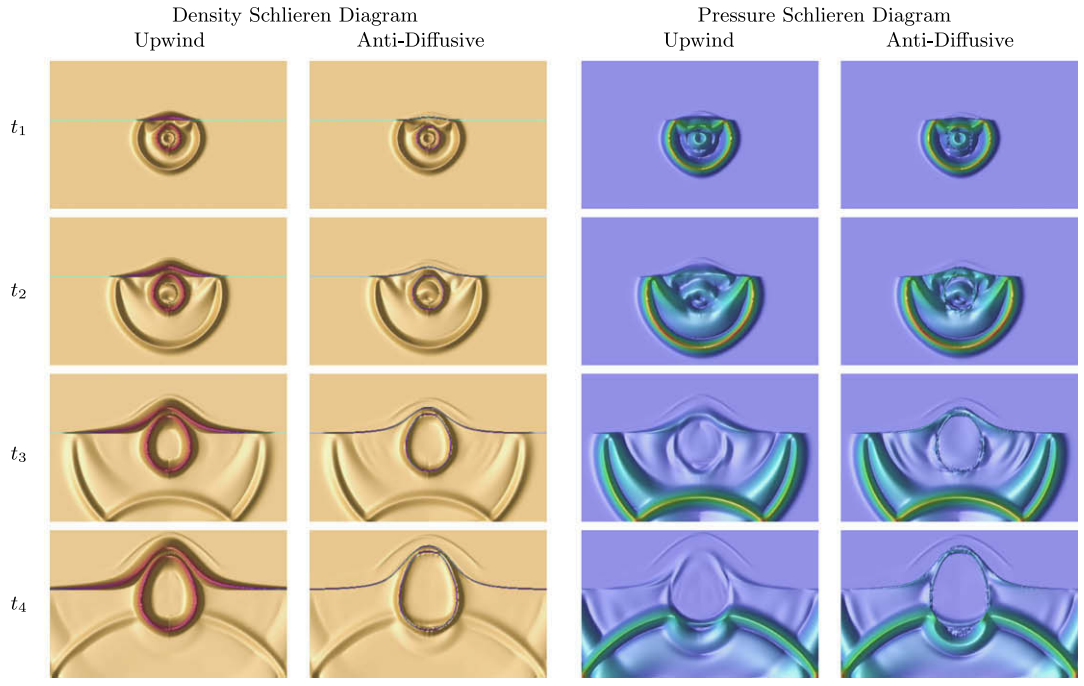

Fig. 27. Underwater explosion test. Profiles at the instants $(t_1, t_2, t_3, t_4) = (0.2, 0.4, 0.8, 1.2)$ ms, of the Schlieren diagram for the density (mapping of $|\nabla\rho|$) and the pressure (mapping of $|\nabla P|$) with both upwind solver and anti-diffusive solvers.

The present test provides rich wave patterns and waves interactions that has been thoroughly analyzed in several previous work (see for example [13,41,40,25] and also [49,12]). Figs. 20 and 21 display Schlieren diagrams obtained with both solvers and allow to observe the evolution several waves. As in [13,25,35] we shall consider the following waves: the incident shock wave (marked with a "×" symbol), the upstream interface position (marked with a "+" symbol), the downstream interface position (marked with a "◇" symbol), which are, respectively, the right-most and the left-most location of the interface at the symmetry axis $x_2 = 44.5$ mm. We also consider the refracted shock wave (marked with a "△" symbol) and the transmitted shock waves (marked with a "▲" and a "*" symbol). The evolution of the fronts position are recorded in space-time diagrams in Fig. 18 which strongly agree with the experimental results [13] and the simulations of [35]. Following as [25,35] we performed a linear least square fit of each set point in order to evaluate the propagation velocity of each

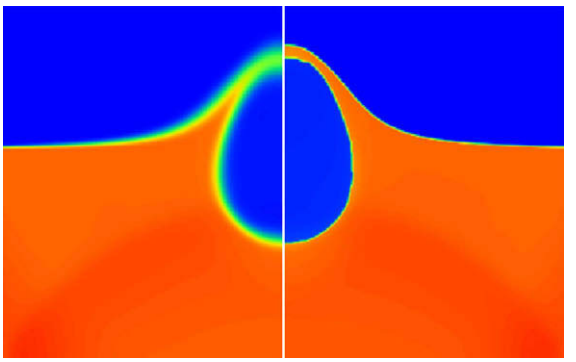

Fig. 28. Underwater explosion test. Comparison of the density profiles at $t = 1.2$ ms, between the upwind solver (left) and anti-diffusive solver (right).

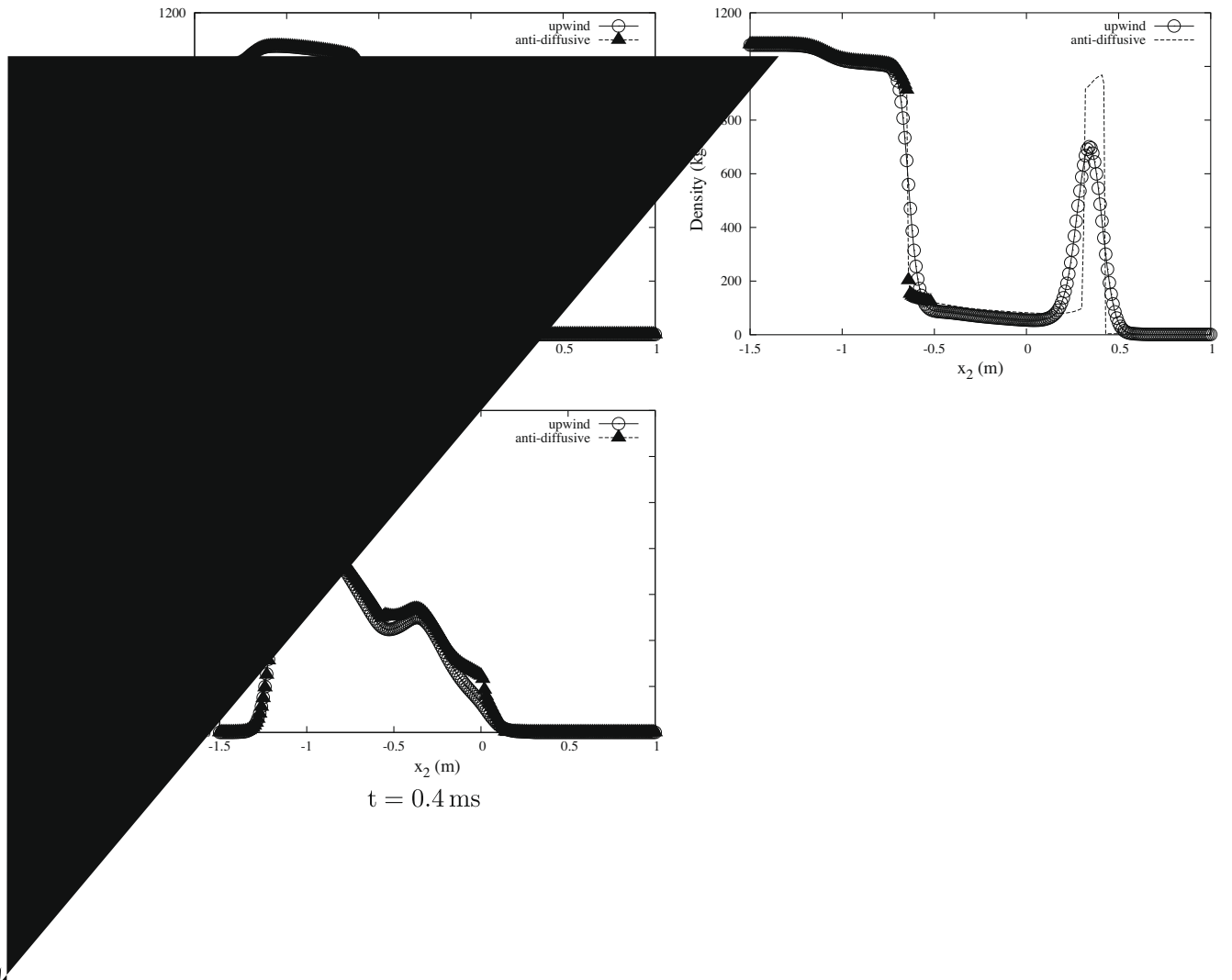

wave. The results are summarized in Table 3 along with the previous simulation results of [25,35] and the experimental results of [13]. The velocity V_s of the incident shock wave is computed for $t \in [0, 250]$ μs, the velocity V_R of the refracted shock wave is measured for $t \in [0, 200]$ μs. The initial and final upstream positions and are measure for, respectively, $t \in [0, 400]$ μs and $t \in [400, 1000]$ μs. The initial and final downstream positions and are measure for, respectively, $t \in [200, 400]$ μs and $t \in [400, 1000]$ μs. The velocity of the transmitted $*$-wave is evaluated for $t \in [200, 259]$ μs. Table 3 shows that a good agreement is found with both the simulations performed in [35] and the experimental results of [13].

Finally, we provide a record of the pressure values at different stations throughout the simulation. Following [25,35] we used the stations located at the distance {3,11,27,43,67,99} mm downstream the gas cylinder along the symmetry axis which corresponds to the points $M_p \in \{(x_1, x_2) \mid x_1 = 197, 189, 173, 157, 133, 101 \text{ mm}, x_2 = 44.5 \text{ mm}\}$. The results are displayed in Fig. 22. One can observe a good agreement between our results and the results computed in [25,35].

5.8. Liquid–gas shock/bubble interaction test

We perform another shock/interface interaction test proposed in [28] that involves a gas bubble surrounded by a liquid. The geometry of the initial condition is depicted in Fig. 23 with the following parameters value:

$$L_1 = 2 \text{ m}, \quad L_2 = 1 \text{ m}, \quad L_s = 0.04 \text{ m}, \quad X_1 = 0.5 \text{ m}, \quad X_2 = 0.5 \text{ m}, \quad r = 0.4 \text{ m}.$$

The gas within the bubble is governed by a perfect gas law while the liquid is modelled with the stiffened gas law (41). The EOS parameters for each material and the fluid state at $t = 0$ are provided in Table 4.

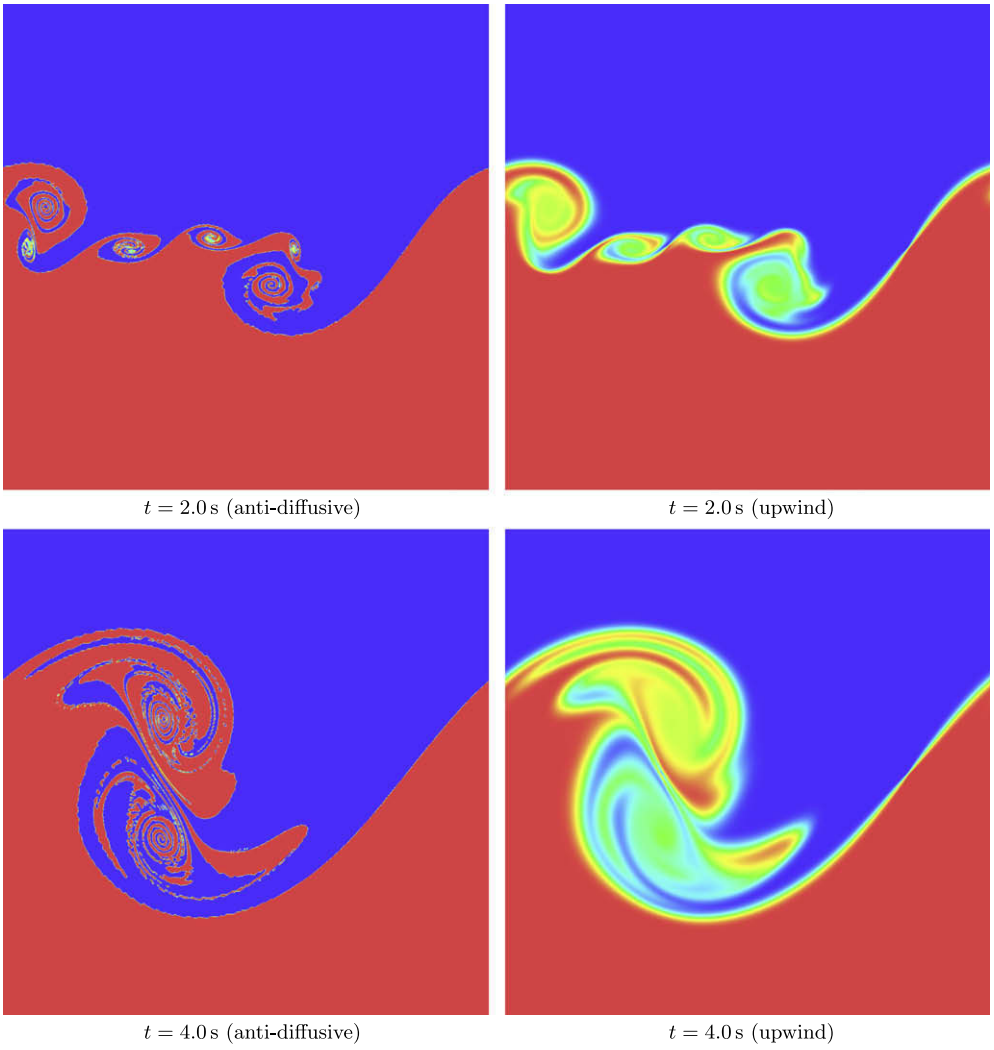

Fig. 30. Kelvin–Helmholtz instability test. Mapping of the color function values obtained with the anti-diffusive scheme and the upwind scheme at instants $t \in \{2.0, 4.0\}$ s.

The computational domain is discretized with a 600×300 grid and we use solid wall boundary conditions for the top and bottom boundaries while we impose constant states at the left and right boundaries. Figs. 24 and 26 display the mapping of, respectively, the color function and the density at several instants. One can clearly see the important variation of the interface topology and more specifically the creation of two symmetrical vortices on each side of the axis $x_2 = 0.5$ m as in [28]. The anti-diffusive feature of the scheme provides sharp profiles for the color function, the mass fraction and the density. At $t = 75$ μs, the number of diffusion cells for the anti-diffusive scheme is 2.74% while it is 19.31% for the upwind scheme. Profiles of cuts along the axis $x_2 = 0.5$ m*s* for the density and the pressure show a good agreement between both scheme far from the interface (see Figs. 25 and 26). The contact discontinuity that appears in the density variable is very sharp. However, one can note that when the waves start interacting with the diffused interface zone for the upwind scheme this induces differences in the density profiles.

5.9. Underwater explosion test

We consider a test presented in [35] for a model of underwater explosion. The phenomena involved in this test have been studied in [41]. The computational domain is the rectangular domain $[-2, 2]$ m $\times$ $[-1.5, 1]$ m. At $t = 0$, the horizontal water surface that separates air and water is located at $x_2 = 0$ and below this line, a bulk of compressed gas lies surrounded by water. This gas bulk has a circular shape with the center $(x_1, x_2) = (0, -3$ m$)$ and a radius $r_0 = 0.12$ m. The liquid in the domain is governed by the stiffened gas law (41) and both air above the water surface and gas inside the bulk are modelled with the same perfect gas law. At $t = 0$, the fluids are at rest in the whole domain. The initial state variables and the EOS

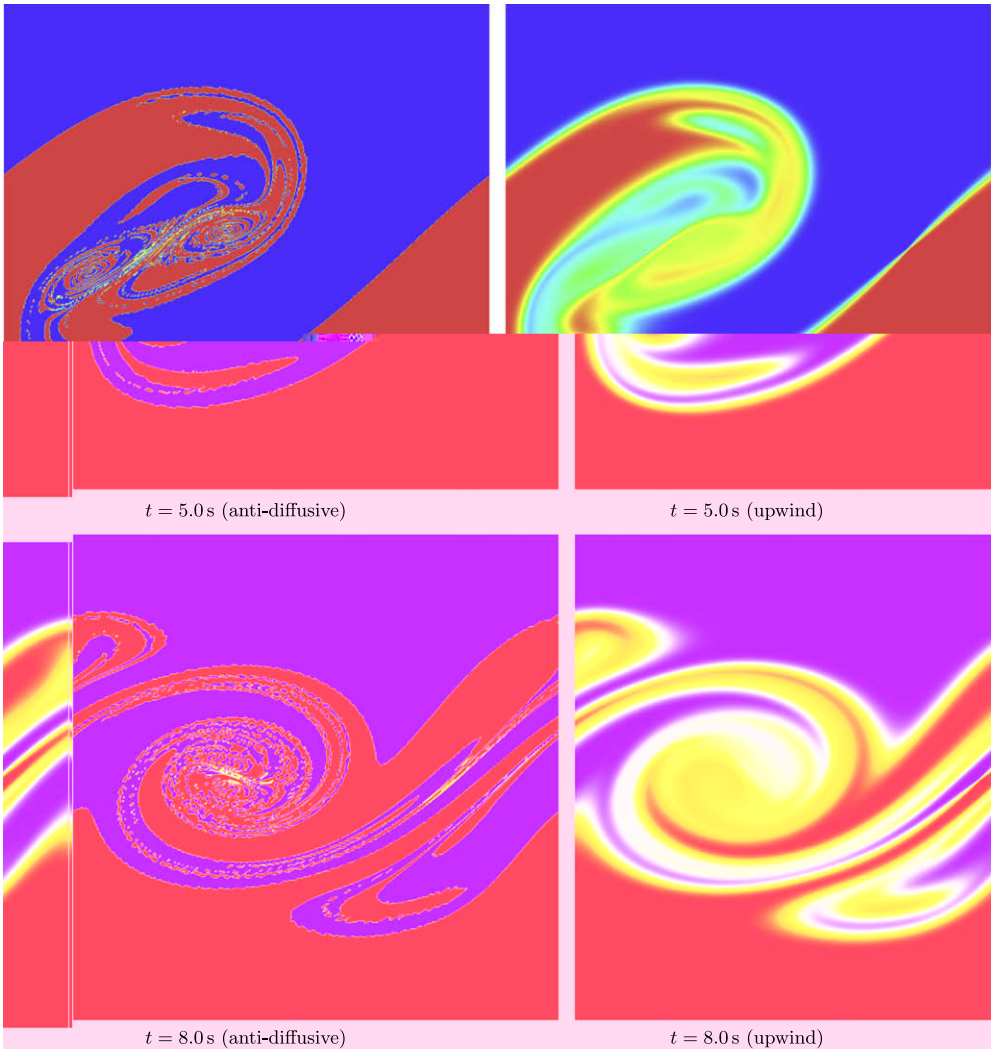

Fig. 31. Kelvin–Helmholtz instability test. Mapping of the color function values obtained with the anti-diffusive scheme and the upwind scheme at instants $t \in \{5.0, 8.0\}$ s.

parameters are provided in Table 5. Gravity effects are neglected and the left, right and bottom boundaries are solid walls, while we impose a transparent boundary condition for the top domain boundary. The domain is discretized with a 400×250 grid. We display the profiles of the Schlieren diagram for the density and the pressure at the instants $t \in \{0.2, 0.4, 0.8, 1.2\}$ ms in Fig. 27. Two circular pressure waves depart from the interface: a shock wave travelling in the water and a rarefaction wave travelling in the gas bulk. As expected (see [41,35]), the gas bulk first starts expanding symmetrically, then as soon as the shock hits the air–water separation, a wave diffraction phenomenon occurs and the shape of the gas bubble evolves into an oval shape. The comparison between the upwind solver and the anti-diffusive solver shows a good agreement (see Fig. 29). The anti-diffusion effect of the solver is clear for the variable y, z and ρ as seen in Figs. 28 and 29. At $t = 1.2$ ms, the number of diffusion cells of the interface for the upwind solver is 15.62% while it is only 0.51% for the anti-diffusive solver.

5.10. Kelvin–Helmholtz instability

We consider the simulation of a Kelvin–Helmholtz instability. The computational domain is a 1 m $\times$ 1 m square containing two perfect gases separated by an interface Γ. We define Γ as a perturbation of the line $x_2 = 0.5$ m in the region $x_1 \in [\alpha, \beta]$, where $0 < \alpha < \beta < 1$. The perturbation is defined by the iso-contour $f(x_1, x_2) = 0$, where the function f reads

$$f(x_1, x_2) = \begin{cases} x_2 + K \sin\left[\pi\left(\frac{x_1-\alpha}{\beta-\alpha}\right)\right], & \text{if } x_1 \in [\alpha, \beta], \\ x_2 - 1/2, & \text{if } x_1 \notin [\alpha, \beta] \end{cases}.$$

For our test, we chose the parameters $(\alpha, \beta, K) = (0.65\ \text{m}, 0.85\ \text{m}, 0.03\ \text{m})$. At $t = 0$, the flow configuration is given by

$$(\gamma, \rho, P, u_1, u_2) = (1.40, 1.0\ \text{kg m}^{-3}, 0.71\ \text{Pa}, +0.25\ \text{m s}^{-1}, 0.0), \quad \text{if } f(x_1, x_2) > 0,$$
$$(\gamma, \rho, P, u_1, u_2) = (1.67, 1.0\ \text{kg m}^{-3}, 0.71\ \text{Pa}, -0.25\ \text{m s}^{-1}, 0.0), \quad \text{if } f(x_1, x_2) \leqslant 0.$$

The discretization is performed with a 1000×1000 grid. We set periodic boundary conditions for the left and right boundaries. Both top and bottom boundaries are solid walls. This test is meant to challenge the ability of the anti-diffusive scheme to deal with very complex variations of the interface geometry while keeping control of the numerical diffusion for the variable z.

Figs. 30 and 31 provide a mapping of the color function values for both anti-diffusive and upwind schemes at several instants. One can see that the overall aspect of the instability is similar with both schemes. However, in regions where the upwind scheme generates $0 < z < 1$ numerical values for the color function, the anti-diffusive scheme creates very fine interface structures that are not destroyed by the numerical diffusion. Moreover, when numerical diffusion seems to extend within the central vortex for the anti-diffusive scheme, it seems to decrease again after few time steps. Let us emphasize that we do not claim that the filaments appearing in the anti-diffusive results are more physically relevant than the shapes obtained with the upwind scheme. Neither do we suggest that the solution has a better resolution — in the sense of a more converged solution — with the anti-diffusive scheme. Indeed, there is no reason to suppose that the velocity field computed by the anti-diffusive scheme is a better resolved velocity field and describes finer vortices than the velocity field computed with the upwind scheme.

As in the previous tests, we see that the anti-diffusive solver succeeds in controlling the diffusion of the color function z (see Fig. 32). After about 11000 time steps the percent of cells with numerically diffused value of z in the domain is 7.54% for

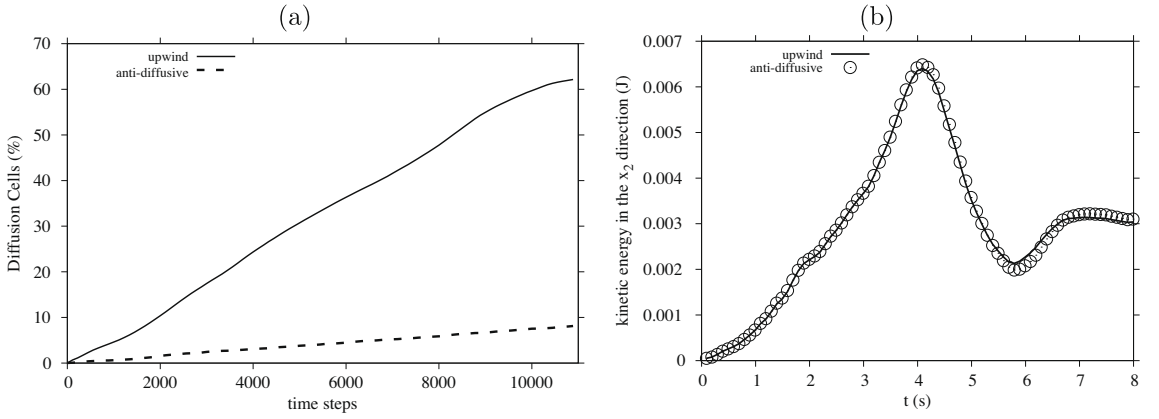

Fig. 32. Kelvin–Helmholtz instability test. (a) Percent of cells in the domain where the color function z is numerically diffused versus the number of time steps, for both upwind and anti-diffusive scheme. (b) Evolution of the kinetic energy in the direction x_2 throughout the computation in norm L^1: graph of the function $t \mapsto \int_{[0,1]^2} \frac{1}{2} \rho u_2^2(x_1, x_2, t) \mathrm{d}x_1 \mathrm{d}x_2$.

the anti-diffusive scheme versus 59.71% for the upwind scheme. As in Section 5.7 the continuous growth of the numerical diffusion is caused by the stretching and break-ups of the interface keeps. The interface length increases as the instability grows and creates therefore more diffusion cells.

We observe a trend of the anti-diffusive scheme towards producing "stairstep" profiles for the interface. The same type of numerical artefacts was observed in [57,56] with the Hyper-C scheme of [44]. This common flaw of both the Hyper-C scheme and the limited downwind scheme of [6] is very critical when the schemes are used for advecting the profile of smooth functions (see [44,7]). In our case we only deal with sharp characteristic functions whose profile are preserved by the numerical scheme. Moreover, the stairstep profile of the interface does not seems to trigger new instabilities that would dramatically alter the growth of the main instability when compared to the upwind results. Indeed, for the sake of comparison, we plotted the evolution of the kinetic energy in the direction, that is perpendicular to the shear in Fig. 32. This figure displays the graph of the function $t \mapsto \int_{[0,1]^2} \frac{1}{2}\rho u_2^2(x_1, x_2, t)\mathrm{d}x_1\mathrm{d}x_2$, which provides a comparison element between the growth rates of the instability computed by both schemes. The match between both approximate solutions is very strong, even for large value of t, far from the linear growth regime.

6. Conclusion

We presented a Lagrange–Remap solver for the five-equation model with isobaric closure examined in [2,3]. This solver was designed following lines similar to [19,7,8]. This method allows to contain the numerical diffusion affecting the color function z that defines the location of the interface between both fluids. Our algorithm does not involve any interface reconstruction process and does not generate extra CPU costs compared to the classical Lagrange–Remap upwind solver. This numerical method does not rely on the analytical form of the EOSs and allows a straightforward use of complex EOSs. The numerical solver is conservative with respect to the mass, momentum, total energy, and partial masses. The numerical fluxes implemented within this scheme are consistent by construction. Under a classical CFL condition, the solver is endowed with stability properties for the color function z and the mass fraction y that are similar to the stability properties of the upwind scheme. In particular, we proved positivity properties regarding both mass fraction and color function. We proved that the numerical scheme preserves constant pressure and velocity profiles similar to those examined in [2,3].

We performed one-dimensional and two-dimensional numerical tests that showed that the discretization of the interface is resolved within a very few transition cells. We verified throughout the tests that the anti-diffusive mechanism is also active for other variables experiencing a jump across the interface like the mass fraction and the density. Far from the interface, the anti-diffusive solver degenerates to the classical Lagrange–Remap upwind. A convergence test was performed on a shock tube test that indicates that the convergence rate of the anti-diffusive solver is at most order 1. Numerical tests involving tabulated EOSs were also achieved. By means of a simple dimensional splitting, we performed two-dimensional tests that concur with the one-dimensional results. Indeed, we observed a good control of the numerical diffusion in the vicinity of the interface and a strong agreement with the upwind solver far from the interface.

The anti-diffusive solver has already been successfully implemented in a three-dimensional parallelized code that is in the process of validation. An extension of the numerical method involving higher order methods is in progress.

Acknowledgments

The authors would like to thank Philippe Hoch (CEA DAM, Bruyères-le-Châtel) and Vincent Faucher (CEA DEN/DANS, Saclay) for their strong support in providing validation data. The authors would also like to thank the reviewers for their thorough reviews, for their patience and comments that helped to significantly improve this article. The present work was partially supported by the Neptune Project, funded by CEA (Commissariat à l'Énergie Atomique), EDF (Électricité de France), IRSN (Institut de Radioprotection et de Sûreté Nucléaire) and AREVA-NP.

References

[1] R. Abgrall, How to prevent pressure oscillations in multicomponent flow calculations: a quasi-conservative approach, J. Comput. Phys. 125 (1996) 150–160.
[2] G. Allaire, S. Clerc, S. Kokh, A five-equation model for the numerical simulation of interfaces in two-phase flows, C.R. Acad. Sci. Paris, Série I 331 (2000) 135–140.
[3] G. Allaire, S. Clerc, S. Kokh, A five-equation model for the simulation of interfaces between compressible fluids, J. Comput. Phys. 181 (2) (2002) 577–616.
[4] I.-L. Chern, J. Glimm, O. McBryan, B. Plohr, S. Yaniv, Front tracking for gas dynamics, J. Comput. Phys. 62 (1986) 10–83.
[5] B. Després, Inégalité entropique pour un solveur conservatif du système de la dynamique des gaz en coordonnées de lagrange, C.R. Acad. Sci. Paris, Série I 324 (1997) 1301–1306.
[6] B. Després, F. Lagoutière, Un schéma non-linéaire anti-dissipatif pour l'équation d'advection linéaire, C.R. Acad. Sci. Paris, Série I 328 (1999) 939–944.
[7] B. Després, F. Lagoutière, Contact discontinuity capturing schemes for linear advection and compressible gas dynamics, J. Sci. Comput. 16 (4) (2001) 479–524.
[8] B. Després, F. Lagoutière, Numerical resolution of a two-component compressible fluid model with interfaces, Prog. Comp. Fluid Dyn. 7 (6) (2007) 295–310.
[9] R. Fedkiw, T. Aslam, B. Merriman, S. Osher, A non-oscillatory Eulerian approach to interfaces in multimaterial flows (the ghost fluid method), J. Comput. Phys. 152 (1999) 457.
[10] J. Glimm, O. McBryan, A computational model for interfaces, Adv. Appl. Math. 6 (1985) 422.
[11] E. Godlewski, P.-A. Raviart, Numerical approximation of hyperbolic systems of conservation laws, Appl. Math. Sci. 118 (1996).

[12] G. Tryggvason, H. Terashima, A front-tracking/ghost-fluid method for fluid interfaces in compressible flows, J. Comput. Phys. 2 (213) (2009) 4012–4037.
[13] J.F. Haas, B. Sturtevant, Interaction of a weak shock wave with cylindrical and spherical gas inhomogeneities, J. Fluid Mech. 181 (1987) 41–76.
[14] C.W. Hirt, B.D. Nichols, Volume of fluid (VOF) method for the dynamics of free boundaries, J. Comput. Phys. 39 (1981) 201.
[15] D. Juric, G. Tryggvason, A front tracking method for dendritic solidification, J. Comput. Phys. 123 (1996) 127.
[16] S. Karni, Multicomponent flow calculations by a consistent primitive algorithm, J. Comput. Phys. 112 (1994) 31–43.
[17] S. Karni, Hybrid multifluid algorithms, SIAM J. Sci. Comput. 17 (5) (1996) 1019–1039.
[18] B. Lafaurie, C. Nardone, R. Scardovelli, S. Zaleski, G. Zanetti, Modelling merging and fragmentation in multiphase flows with SURFER, J. Comput. Phys. 113 (1994) 134–147.
[19] F. Lagoutière, Modélisation mathématique et résolution numérique de problèmes de fluides compressibles à plusieurs constituants, Ph.D. Thesis, Université Paris VI, 2000.
[20] J. Massoni, R. Saurel, B. Nkonga, R. Abgrall, Proposition de méthodes et modèles eulériens pour les problèmes à interfaces entre fluides compressibles en présence de transfert de chaleur, Int. J. Heat Mass Transfer 45 (6) (2001) 1287–1307.
[21] A. Murrone, H. Guillard, A five equation reduced model for compressible two phase flow problems, J. Comput. Phys. 202 (2) (2005) 664–698.
[22] S. Osher, P. Smereka, A level set approach for computing solutions to incompressible two-phase flow, J. Comput. Phys. 114 (1994) 146–159.
[23] D. Peng, B. Merriman, S. Osher, H. Zhao, M. Kang, A PDE based fast local level set method, J. Comput. Phys. 155 (1999) 410–438.
[24] G. Perigaud, R. Saurel, A compressible flow model with capillary effects, J. Comput. Phys. 209 (1) (2005) 139–178.
[25] J.J. Quirk, S. Karni, On the dynamics of a shock-bubble interaction, J. Fluid Mech. 318 (1996) 129–163.
[26] P.L. Roe, Approximate riemann solvers, parameter vectors, and difference schemes, J. Comput. Phys. 43 (1981) 357–372.
[27] R. Saurel, R. Abgrall, A multiphase Godunov method for compressible multifluid and multiphase flows, J. Comput. Phys. 150 (1999) 425–467.
[28] R. Saurel, R. Abgrall, A simple method for compressible multifluid flows, SIAM J. Sci. Comput. 21 (3) (1999) 1115–1145.
[29] R. Scardovelli, S. Zaleski, Direct numerical simulation of free-surface and interfacial flow, Ann. Rev. Fluid Mech. 31 (1999) 567–584.
[30] J.A. Sethian, Level Set Methods: Evolving Interfaces in Geometry, Fluid Mechanics, Computer Vision and Materials Sciences, Cambridge University Press, 1996.
[31] J.A. Sethian, Level Set Methods and Fast Marching Methods: Evolving Interfaces in Computational Geometry, Fluid Mechanics, Computer Vision and Materials Science, Cambridge University Press, Cambridge, 1999.
[32] K.M. Shyue, An efficient shock-capturing algorithm for compressible multicomponent problems, J. Comput. Phys. 142 (1998) 208–242.
[33] K.M. Shyue, A fluid-mixture type algorithm for compressible multicomponent flow with van der Waals equation of state, J. Comput. Phys. 156 (1999) 43–88.
[34] K.M. Shyue, A fluid-mixture type algorithm for compressible multicomponent flow with Mie-Gruneisen equation of state, J. Comput. Phys. 171 (2001) 678–707.
[35] K.M. Shyue, A wave-propagation based volume tracking method for compressible multicomponent flow in two space dimensions, J. Comput. Phys. 215 (2006) 219-–244.
[36] J. Strain, Fast tree-based redistancing for level set computations, J. Comput. Phys. 152 (1999) 664–686.
[37] G. Allaire, S. Kokh, Test-case no. 19: shock-bubble interaction, Multiphase Sci. Technol. 16 (2004) 117–120.
[38] S. Dellacherie, Numerical resolution of a potential diphasic low mach number system, J. Comput. Phys. 223 (1) (2007) 151–187.
[39] O. Desjardins, V. Moureau, H. Pitsch, An accurate conservative level set/ghost fluid method for simulating turbulent atomization, J. Comput. Phys. 227 (2008) 8395–8416.
[40] Z. Ding, S.M. Gracewski, The behavior of a gas cavity impacted by a weak or strong shock wave, J. Fluid Mech. 309 (1996) 183–209.
[41] J.W. Grove, R. Menikoff, Anomalous reflection of a shock wave at a fluid interface, J. Fluid Mech. 219 (1990) 313–336.
[42] D. Henright, R. Fedkiw, J. Ferziger, I. Mitchell, A hybrid particle level set method for improved interface capturing, J. Comput. Phys. 183 (2002) 83–116.
[43] S. Kokh, F. Lagoutière, An anti-diffusive method for simulating compressible two-phase flows with interfaces, in: R. Eymard, J.M. Hérard (Eds.), Finite Volumes for Complex Applications, V, Wiley-ISTE, 2008, pp. 519–526.
[44] B.P. Leonard, The ultimate conservative difference scheme applied to unsteady one-dimensional advection, Comput. Meth. Appl. Mech. Eng. 88 (1) (1991) 17–74.
[45] T.G. Liu, C. Khoo, The accuracy of the modified ghost fluid method for gas–gas riemann problem, Appl. Numer. Math. 57 (2007) 721–733.
[46] T.G. Liu, C. Khoo, K.S. Yeob, Ghost fluid method for strong shock impacting on material interface, J. Comput. Phys. 190 (2003) 651–681.
[47] W. Mulder, S. Osher, J.A. Sethian, Computing interface motion in compressible gas dynamics, J. Comput. Phys. 100 (2) (1992) 209–228.
[48] D. Nguyen, F. Gibou, R. Fedkiw, A fully conservative ghost fluid method & stiff detonation waves, in: 12th Int. Detonation Symposium, San Diego, CA, 2002.
[49] R.R. Nourgaliev, T.N. Dinh, T.G. Theofanous, Adaptive characteristics-based matching for compressible multifluid dynamics, J. Comput. Phys. (2006) 500-–529.
[50] E. Olsson, G. Kreiss, A conservative level set method for two phase flow, J. Comput. Phys. 210 (2005) 225–246.
[51] E. Olsson, G. Kreiss, S. Zahedi, A conservative level set method for two phase flow ii, J. Comput. Phys. 225 (2007) 785–807.
[52] G. Russo, P. Smereka, A remark on computing distance functions, J. Comput. Phys. 163 (2000).
[53] G.A. Sod, A survey of several finite difference methods for systems of nonlinear hyperbolic conservation laws, J. Comput. Phys. (1978) 1–31.
[54] M. Sussman, E. Fatemi, An efficient, interface-preserving level set redistancing algorithm and its application to interfacial incompressible fluid flow, SIAM J. Sci. Comput. 20 (1999) 1165–1191.
[55] P.K. Sweby, High resolution schemes using flux limiters for hyperbolic conservation laws, SIAM J. Numer. Anal. 21 (5) (1984) 995–1011.
[56] O. Ubbink, Numerical Predication of Two-Fluid System with Sharp Interfaces, Ph.D. Thesis, University of London, 1997.
[57] O. Ubbink, R.I. Issa, A method for capturing sharp fluid interfaces on arbitrary meshes, J. Comput. Phys. 153 (1) (1999) 26–50.
[58] E.H. van Brummelen, B. Koren, A pressure-invariant conservative Godunov-type method for barotropic two-fluid flows, J. Comput. Phys. 185 (2003) 289–308.
[59] S.O. Unverdi, G. Tryggvason, A front tracking method for viscous, incompressible, multifluid flows, J. Comput. Phys. 100 (1992) 25.